Contractile ring mechanosensation and its anillin-dependent tuning during early embryogenesis

Christina Rou Hsu[1,2,3], Gaganpreet Sangha[1,2,3], Wayne Fan[1,2], Joey Zheng[1,2], and Kenji Sugioka[1,2*]

[1]Life Sciences Institute, The University of British Columbia, 2350 Health Sciences Mall, Vancouver, BC V6T1Z3, Canada

[2]Department of Zoology, The University of British Columbia, 2350 Health Sciences Mall, Vancouver, BC V6T1Z3, Canada

[3]These authors are equally contributed.

***Corresponding author**

Kenji Sugioka

Life Sciences Institute, Department of Zoology, The University of British Columbia, 2350 Health Sciences Mall, Vancouver, BC V6T1Z3, Canada

sugioka@zoology.ubc.ca

Phone: +1-604-404-3150

Abstract

The contractile ring plays crucial roles in animal morphogenesis. Previous studies have explored how tissue mechanics controls the contractile ring; however, the mechanisms by which the ring senses tissue mechanics remain largely unknown. Here, we demonstrate the mechanism of contractile ring mechanosensation and its tuning during asymmetric ring closure of *Caenorhabditis elegans* embryos. High-resolution imaging of cortical flow revealed that local suppression of the ring-directed cortical flow is associated with a delay in furrowing. This suppression of cortical flow results from cortical compression. We found that the artificial inhibition of ring-directed cortical flow was sufficient to induce asymmetric ring closure in symmetrically dividing cells. Moreover, genetic analysis suggests that the positive feedback loop among ring-directed cortical flow, myosin enrichment, and ring constriction constitutes the anillin-dependent, mechanosensitive engine driving asymmetric ring closure. Our results suggest that the balance between RhoA-dependent and cortical flow-dependent myosin enrichment fine-tunes the ring's mechanosensitivity in tissues.

Introduction

The cytokinetic contractile ring plays crucial roles in morphogenesis during asymmetric cell division and epithelial morphogenesis. Previous studies have shown that intracellular and extracellular mechanics can influence contractile ring positioning, but how the contractile ring senses these mechanical cues remains largely unknown [1–3]. One important model system to study contractile ring mechanosensation is the asymmetric ring closure found in animal zygotes and epithelial tissues, termed unilateral or asymmetric cytokinesis [4,5]. Unilateral cytokinesis is ubiquitously observed in both invertebrates and vertebrates, including humans [6–10], and its dysregulation has been associated with reduced cytokinesis resilience, disrupted epithelial integrity, and defective lumen morphogenesis[6,11,12].

Contractile ring assembly is regulated by the activation of small GTPase RhoA. The mitotic spindle plays a central role in specifying the site of RhoA activation through the centralspindlin complex [13–16]. The activated RhoA then induces Rho-associated kinase (ROCK)-dependent myosin activation, as well as formin-dependent actin assembly, to initiate contractile ring formation [17–19]. Furthermore, the centrosome and astral microtubules at the polar region suppress ring assembly [20–27]. Pioneering studies have shown that asymmetric spindle positioning is sufficient to induce asymmetric ring closure in a few examples such as ctenophore zygotes and normally symmetrically-dividing sea urchin embryos, [28,29] and that the spindle-cortex proximity asymmetrically activates RhoA [30].

Conversely, unilateral cytokinesis in various vertebrate and invertebrate epithelial tissues and in the *C. elegans* zygote is spindle positioning-independent. In both systems,

62 the mere spindle-cortex proximity does not dictate the leading edge of the ring[6,31–34]. In
63 *Drosophila* embryonic and follicular epithelia, adherens junctions regulate asymmetric
64 ring closure [2,34]. In this system, passive mechanical resistance imposed by adherens
65 junctions anchors the contractile ring at the apical cell cortex. In contrast, unilateral
66 cytokinesis in the *C. elegans* zygote is regulated by contractile ring components anillin
67 and septin[6]. In this system, contractile ring components enrich at the leading edge,
68 forming a structurally asymmetric ring. However, the precise mechanisms of asymmetric
69 ring closure remain unclear in both systems. In *C. elegans* zygotes, knockdowns of anillin
70 and septin disrupt the asymmetric ring closure [6]; however, the *ani-1(RNAi)* phenotype is
71 rescued in a mutant background of a worm-specific RhoA activator, NOP-1 [35].
72 Furthermore, anillin and septin are dispensable for asymmetric ring closure at least in
73 *Drosophila* embryonic and adult dorsal thorax epithelial cells, leaving the role of anillin
74 cryptic [2,36].
75 Recent studies show that cortical flow, a concerted flow of cell cortex materials at
76 the cell surface, facilitates contractile ring assembly through cortical compression[37–39].
77 Therefore, we hypothesized that the contractile ring utilizes this mechanism to sense
78 tissue mechanics. To elucidate the mechanism of contractile ring mechanosensation, we
79 performed high-resolution 4D imaging. By developing analysis pipelines measuring
80 various parameters such as ring closure, ring eccentricity, cortical flow, and myosin
81 enrichment rate from the same datasets, we gained an integrative view of
82 mechanochemical contractile ring regulation during asymmetric ring closure.
83 Quantitative analysis of these parameters suggests that the furrowing delay at the lagging
84 cell cortex is induced by the mechanical retardation of cortical flow towards the ring. By

conducting an *in vitro* cell-bead adhesion assay, we artificially reduced the ring-directed cortical flow, thereby confirmed the role of ring-directed cortical flow in asymmetric contractile ring closure. Finally, through a genetic analysis, we identified the molecular pathway that tunes contractile ring mechanosensitivity.

Results

High-resolution 4D imaging and quantitative analysis of contractile ring dynamics

To better understand the mechanism of asymmetric ring closure, we performed high-resolution 4D imaging of GFP-fused non-muscle myosin II (NMY-2) in *C. elegans* zygotes (Figures 1A and S1A). We applied a new imaging method combining the use of spacer beads and a refractive index-matching sample medium to avoid the previously reported compression-dependent cell rotation [40,41] and to improve image resolution [42], respectively (see Methods for detail). These improvements allowed us to capture uncompressed embryonic volumes (30 μm thickness) at 5.6-s intervals with a 1 μm step size, without cell rotation (Figure S1B and Movie S1).

We developed image analysis pipelines to quantify the dynamics of contractile ring closure (Figures 1B and S1A). First, we performed image segmentation to computationally detect the contractile ring (Figures 1B and S1C). Using the segmentation data, we measured the ring radius and ring center coordinates at every time point. From these measurements, we calculated the ring closure indices $R_{closure}(t)$ (with 1.0 representing complete closure), ring eccentricities $E(t)$ (indicating off-center tendency), and the degrees of leading-edge and lagging-edge advancement towards the cell center $L_{lead}(t)$, $L_{lag}(t)$ (Figure 1D). Due to the natural variations in cytokinesis timing, we aligned

108 the time series data relative to the time around 10% contractile ring closure (Figure S1D).
109 We also defined cytokinesis onset based on the extrapolation of an initial linear part of
110 the ring closure curve to 0 (Figure S1D). Markedly, the newly developed imaging and
111 quantification methods allowed us to detect differences in sub-percentage ring closure
112 indices. The data obtained show that the contractile ring initially undergoes nearly the
113 upper limit of eccentric closure (Figure 1E; Movie S1), and unilateral furrow ingression
114 continues until the start of lagging edge furrowing (Figure 1E–F). These data indicate that
115 the primary factor contributing to ring off-centering is the time interval between the
116 onsets of furrowing at the leading edge and the lagging edge (Figure 1F; 0-117 sec).
117

118 **Ring closure velocity and a delay in lagging edge furrowing determine the ring**
119 **eccentricity**

120 We analyzed the relationship among peak eccentricity, time lag between leading
121 and lagging edge advancement, and ring closure velocity. The time lag, Δt, was
122 determined by the delay between the leading and lagging edges reaching 10%
123 advancement relative to the initial ring diameter (Figure 1F–G). Additionally, ring
124 closure velocity, *v*, was calculated based on the slope of the $R_{clousre}$ curve between 20%
125 and 70% closure points (Figure 1G). We found that ring closure velocity and peak
126 eccentricity have no clear correlation (Pearson's r = 0.352, p = 0.028, n = 39; Figure 2A).
127 On the contrary, the time lag is weakly correlated with the peak eccentricity (Pearson's r
128 = 0.54, p = 0.0003, n = 39; Figure 2A). Since a slowly closing ring might have a longer
129 time lag than a faster one, we calculated the normalized time lag, Δt_n, by multiplying the
130 ring closure velocity by the time lag (Figure 2B). We found that the normalized time lag

131 is strongly correlated with peak eccentricity (Pearson's r = 0.93, $p < 0.0001$, n = 39;
132 Figure 2B), indicating that both ring closure velocity and time lag control asymmetric
133 ring closure in normal cells.

134 To investigate whether ring closure velocity and time lag generally control
135 eccentricity, we analyzed these parameters in mutants or RNAi knockdowns of
136 actomyosin regulators (Figures 2C–G and S2A–F). In addition to the previously reported
137 ANI-1/Anillin, we found that POD-1/Coronin and MLC-4/myosin regulatory light chain
138 are required for ring eccentricity (Figure 2C–D). We also confirmed that a deletion
139 mutation of the worm-specific RhoA activator NOP-1 rescued the *ani-1(RNAi)* phenotype
140 [35] and that the knockdown of LET-502/ROCK did not cause eccentricity defects [6], as
141 reported previously (Figure 2C–D).

142 We calculated time lag, ring closure velocity, and normalized time lag in these
143 conditions. Time lag (raw values) and peak eccentricity were not particularly correlated
144 (Pearson's r = 0.54, $p = 0.21$; Figure S2G). However, we found that normalized time lag
145 is strongly correlated with peak eccentricity (Pearson's r = 0.99, $p < 0.0001$; Figure 2E).
146 The relationship between ring closure velocity and time lag also shows that conditions
147 with asymmetric closure and symmetric closures are separated within the parameter
148 space (Figure 2F). Therefore, cells that exhibit faster ring closure and longer time lag
149 tend to display asymmetric ring closure. Using these data, we investigated why the *nop-1*
150 mutation was able to rescue the *ani-1(RNAi)* phenotype. We found that the *nop-1*
151 mutation increased both time lag and ring closure velocity compared to *ani-1(RNAi)*
152 alone (Figure 2G), suggesting that the rescue is due to the increase of these parameters.

153 These results suggest that ring eccentricity is collectively determined by the ring closure
154 velocity and a delay in furrowing at the lagging edge.
155
156 **Reduced ring-directed cortical flow at the lagging cell cortex accompanies**
157 **circumferential-axis cortical flow**
158 We analyzed the mechanism of the lagging edge furrowing delay. As ring-directed
159 cortical flow is proposed to contribute to the positive feedback regulation of the
160 contractile ring assembly (Figure 3A)[37], we hypothesized that the delay is due to the
161 feedback loop having lower activity at the lagging edge than at the leading edge. To test
162 this hypothesis, we analyzed cortical flow at the leading and lagging cortices using
163 particle image velocimetry (PIV) [43] (Figures 3B and S3, and Movie S2).
164 First, we analyzed the mechanism of ring-directed cortical flow generation, which
165 is an unclear part of the proposed feedback model. Cortical flow is a phenomenon driven
166 by a gradient in actomyosin contractility [44]. This gradient is established during
167 cytokinesis, with higher contractility at the equator and relaxation at the pole [23,37,38].
168 Given that the contractility gradient continues to exist during ring assembly and closure,
169 the ring should consistently pull the cell cortex from the polar region. To confirm this
170 prediction, we plotted velocities of ring edge advancement (Figure 3C; solid lines) and
171 ring-directed cortical flow (Figure 3C; dotted lines) and found that they correlate well
172 both at the leading and lagging edges (leading edge: Pearson's r = 0.77, $p < 0.0001$,
173 lagging edge: Pearson's r = 0.89, $p < 0.0001$). Furthermore, ring closure velocity and
174 peak ring-directed flow are highly correlated in different RNAi and mutant conditions,
175 including *ani-1(RNAi)* (Figure 8D; Pearson's r = 0.94, $p = 0.002$). These results suggest

176 that the invaginating ring edge consistently pulls the nearby cell cortex to generate ring-
177 directed cortical flow to form a positive feedback loop (Figure 3A).
178 Next, we analyzed the difference in cortical flow between leading and lagging
179 cortices. To better understand the influx of the cortical flow within the equatorial region,
180 we calculated the convergence of cortical flow vectors along the A-P axis and the
181 orthogonal, circumferential-axis (Figure 3B). Furthermore, we tracked myosin foci to
182 confirm the PIV data (Figure 3E). At the leading cell cortex, A-P axis convergence
183 increased rapidly and reached to its peak before the onset of lagging edge furrowing
184 (Figure 3D; left). Consistently, myosin foci tracking showed continuous ring-directed
185 cortical flow (Figure 3D; top). Conversely, A-P axis convergence in the lagging cell
186 cortex decreased shortly after cytokinesis onset and reached a local minimum before the
187 onset of lagging edge furrowing (Figure 3D; left, Figure 3E; $t_n = 58$). During this period,
188 we observed increase in circumferential axis convergence only at the lagging cell cortex
189 (Figure 3D; right). These results suggest that circumferential-axis cortical flow negatively
190 correlates with ring-directed cortical flow.
191
192 **Cells undergoing asymmetric ring closure exhibit polarized mechanical loading at**
193 **the lagging cortex**
194 Circumferential cortical flow could inhibit ring-directed cortical flow, potentially through
195 a mechanical process (Figure 3A). To infer cortical mechanics from the flow vectors, we
196 used cortical convergence. Before furrowing onset, convergence at the surface signifies
197 cortical compression (Figure 4A, top). After the onset of furrow ingression, convergence

198 at the surface represents the sum of cortical compression and ingression, similar to how
199 converging surface sea water sinks towards the ocean floor (Figure 4B, bottom).
200 In control embryos, we observed that ring-directed cortical compression at the
201 lagging cell cortex decreased upon cytokinesis onset (Figures 4B; top left). However, this
202 decline was not apparent in *ani-1(RNAi)* (Figure 4B; top middle). The decline reemerged
203 with the introduction of a *nop-1* mutation (Figure 4B; top right). On the other hand, there
204 were no marked differences in circumferential axis convergence under these conditions
205 (Figure 4B; bottom row). The rate of reduction in ring-directed cortical compression,
206 estimated from the lines connecting local maxima and minima (red and blue arrowheads
207 in the Figure 4B), also confirmed a similar relationship (Figure 4C). We found that
208 conditions with asymmetric ring closure (control, *ani-1;nop-1*, and *let-502*) and
209 symmetric ring closure (*ani-1* and *nop-1*) exhibited a reduction and no change in ring-
210 directed compression, respectively (Figure 4C). Since control and *ani-1(RNAi)* displayed
211 a similar ring closure velocity (Figure 2F), the observed cortical relaxation cannot be
212 attributed to the ring closure rate. In contrast, peak circumferential-axis convergence
213 strongly correlates with ring closure velocity (Pearson's r = 0.90, p = 0.005) (Figure 4D–
214 E). These results suggest that in general, contractile ring closure induces circumferential
215 axis compression. This compression is then accompanied by reduced ring-directed
216 compression in cells undergoing asymmetric ring closure (Figure 4F). However, ring-
217 directed compression in *ani-1(RNAi)* does not respond to the compression along the
218 circumferential axis.
219
220 **Non-ring-directed cortical compression suppresses ring-directed cortical flow**

221 We hypothesized that any non-ring-directed cortical compression, like the
222 circumferential-axis compression we observed, inhibits ring-directed cortical flow. To
223 test this hypothesis, we induced ectopic cortical compression using a semi-dominant
224 temperature-sensitive mutation of actin, *act-2(or295)*, known to cause actin filament
225 stabilization and ectopic cortical contractility [45] (Figure 5A). In normal cells, the leading
226 cortex demonstrates consistent ring-directed flow, while the lagging cortex experiences a
227 period of delay followed by ring-directed flow (Figure 5A–B). In *act-2(or295)*, ring-
228 directed movement of myosin foci was suppressed during contraction and pronounced
229 during relaxation (Figure 5C). Ring closure is necessary for relaxation-induced ring-
230 directed cortical flow, as similar flow was not observed post-cytokinesis (Figure 5D).
231 These results suggest that non-ring-directed cortical compression inhibits ring-directed
232 cortical flow at the lagging cell cortex (Figure 5E).
233

234 **Non-ring-directed compression delays ring edge advancement without suppressing**
235 **ring constriction**

236 A previous study demonstrated that laser-induced ablation of the cell cortex behind the
237 ring did not accelerate the ring closure rate [37]. This suggests that ring closure is not
238 constrained by the mechanical resistance of the cell cortex behind the ring. If this is
239 indeed the case, the observed retardation of ring-directed flow would not limit the ring
240 closure rate, and therefore, would not influence the ring eccentricity. We tested this
241 possibility using highly contractile *act-2(or295)* mutants and found that the overall ring
242 closure curves were similar to those of the control, with the ring velocity even exceeding
243 than the control (Figure 2F). This confirms the first part of our prediction. However, the

244 contractile rings of the *act-2* mutant frequently displayed oscillatory movement during
245 constriction and exhibited a lower mean peak eccentricity compared to the control
246 (Figures 6A and 2D). These results suggest that cortical compression influences ring
247 position without altering the constriction rate.

248 We investigate how cortical compression behind the ring affects ring positioning.
249 To infer cortical compression, we measured myosin intensity changes at the cell surface
250 closest to the objective lens (referred to as the top surface) (Figure 6B). The upward and
251 downward movements of contractile ring along the top-bottom axis were also measured
252 using the same samples (Figure 6B). During contraction at the top surface, the downward
253 movement of the top ring edge was often halted, as though the top ring edge were
254 anchored (Figure 6C–E; labeled as "contraction," Movie S3). Conversely, relaxation of
255 the top surface often coincided with the bottomward movement of the top ring edge
256 (Figure 6C–E; labeled as "relaxation," Movie S3). Quantitative analysis of cortical
257 compression and acceleration of the top ring edge also confirmed these trends (Figure
258 6F–H; positive acceleration indicates movement towards the bottom surface). These
259 findings suggest that cortical compression behind the ring impedes the advancement of
260 the nearby ring edge.

261 How does the compression-dependent retardation of the ring edge occur without
262 delaying the overall ring constriction rate? Notably, we frequently observed upward
263 movement of the bottom ring edge when the top surface is compressed (Figure 6C–E, I).
264 Thus, it is likely that when a certain part of the ring edge advancement is prevented, other
265 areas of the ring edge pull more cortex from the nearby surface, maintaining a similar
266 constriction rate.

267

268 **Artificial inhibition of ring-directed cortical flow is sufficient to induce ring**

269 **eccentricity**

270 Our data suggest that the retardation of ring-directed cortical flow can trigger asymmetric

271 ring closure. To directly test this hypothesis, we inhibited ring-directed cortical flow in

272 symmetrically dividing cells. It is known that the two-cell stage AB cell undergoes

273 asymmetric ring closure, similar to the P_0 zygote [46] (Figures 7A and S5). We found that

274 unilateral ring closure requires cell contact with the neighboring P_1 cell (Figure 7B–C).

275 To inhibit ring-directed cortical flow, we attached adhesive polystyrene beads to the

276 symmetrically dividing isolated AB cell (Figure 7D–E). The beads, which were coated

277 with positively charged Rhodamine fluorescent dyes and salts, adhere to the plasma

278 membrane. This adhesion is presumed to occur through electrostatic interaction, similar

279 to the mechanism observed with poly-L-lysine coating. As shown in our previous study,

280 attachment of the 30 μm diameter beads reduced ring-directed flow in the area proximal

281 to the bead attachment site (Figure 7E) [1]. The response scaled with the bead diameter,

282 suggesting that passive mechanical resistance imposed by adhesive beads limits ring-

283 directed flow (Figure 7E). Notably, the attachment of the 30 μm beads increased peak

284 eccentricity, and about 50% of the cells exhibited a level of ring eccentricity comparable

285 to that of the intact AB cell *in vivo* (Figure 7C, F–H). Thus, we conclude that mechanical

286 retardation of ring-directed cortical flow is sufficient to induce asymmetric ring closure.

287

288 **Anillin tunes contractile ring mechanosensitivity**

289 Our analysis suggests that contractile rings in both the P_0 zygote and the two-cell stage
290 AB cell exhibit mechanosensitivity. We found that *ani-1(RNAi)* embryos exhibited
291 reduced ring eccentricity in both cell types, whereas *pod-1(RNAi)* showed defects only in
292 P_0 (Figure 8A; top panel). The observed loss of asymmetric closure in *pod-1(RNAi)* can
293 be explained by reduced circumferential-axis convergence (Figure 4D and 8A). These
294 results suggest that the contractile ring in *pod-1(RNAi)* retains its mechanosensitivity but
295 lacks the P_0 mechanical cue. Conversely, *ani-1(RNAi)* embryos had a normal level of
296 circumferential-axis convergence (Figure 4D and 8A), indicating that the contractile rings
297 in *ani-1(RNAi)* have impaired mechanosensitivity.

298 We observed that contractile rings in *ani-1(RNAi)* often retain a unusually high
299 level of myosin signal (Figure 8B). Indeed, the myosin enrichment rate in *ani-1(RNAi)* is
300 greater than any of the other RNAi groups that we tested (Figure 8C). Therefore, we
301 reasoned that the ectopic enrichment of myosin might disrupt the mechanosensitivity of
302 the *ani-1(RNAi)* ring. We hypothesized that a cortical flow-dependent positive feedback
303 loop in the contractile ring assembly sensitizes the contractile ring to mechanical stresses,
304 and that the feedback loop is disrupted in *ani-1(RNAi)* embryos (Figure 8G; central box).

305 We observed a strong correlation between ring closure velocity and peak ring-
306 directed cortical flow across different RNAi/mutant groups including *ani-1(RNAi)*, as
307 described above (Figure 8D). We also found that the myosin enrichment rate is highly
308 correlated with ring closure velocity and peak ring-directed cortical flow among sample
309 groups excluding *ani-1(RNAi)* (Figure 8E: Pearson's $r = 0.93$, $p < 0.007$, Figure 8F:
310 Pearson's $r = 0.84$, $p < 0.03$). Conversely, *ani-1(RNAi)* exhibited excess myosin
311 enrichment rate relative to the ring closure velocity and peak ring-directed cortical flow

312 (Figure 8E–F). These results suggest that the positive feedback loop between ring-
313 directed cortical flow, myosin enrichment, and ring constriction was disrupted in *ani-*
314 *1(RNAi)* embryos.

315 We further observed that the *nop-1* mutation rescued the asymmetric ring closure
316 defects in *ani-1(RNAi)* in both the P_0 and AB cells (Figure 8A), indicating that the *nop-1*
317 mutation restored the impaired mechanosensitivity of the contractile ring. The rescue of
318 polarized mechanical loading also supports this idea (Figure 4B–C). Analysis of myosin
319 levels revealed that the *nop-1* mutation reduced the ectopic myosin enrichment rate in
320 *ani-1(RNAi)* (Figure 8B–C). As a result, *ani-1(RNAi); nop-1(it142)* embryos regained a
321 normal level of myosin enrichment relative to ring closure velocity and peak ring-
322 directed flow (Figure 8D–F). Therefore, we concluded that impairment of the contractile
323 ring's mechanosensitivity is due to the disruption of the positive feedback loop caused by
324 excessive myosin enrichment.

325

326 **Discussion**

327 In this study, we have identified the mechanisms underpinning contractile ring
328 mechanosensation and the tuning of mechanosensitivity. Previous studies have shown
329 that ring-directed cortical compression promotes ring assembly, but our findings
330 demonstrate that non-ring-directed compression slows down ring-directed cortical flow
331 and the advancement of the ring edge. The suppression of ring-directed cortical flow was
332 sufficient to induce asymmetric ring closure in symmetrically dividing cells. The
333 mechanism of ring mechanosensation relies on a normal rate of myosin enrichment, in
334 relation to the velocities of ring closure and cortical flow. Finally, our results show that

335 anillin is required for the sensitization of the contractile ring against intercellular and
336 intracellular mechanics.

337 Based on our analysis and previous studies, we propose a cortical flow-dependent
338 contractile ring mechanosensation model (Figure 8G). The critical component of the
339 model is the positive feedback loop among ring constriction, ring-directed cortical flow,
340 and myosin enrichment. Khaliulin et al. (2018) proposed this feedback loop in the
341 contractile ring constriction process based on correlations among these parameters in
342 normal zygotes [37]. Our study further confirms these correlations in RNAi and mutant
343 backgrounds with varying ring closure velocities (Figure 8D–F). In our model,
344 intracellular and intercellular mechanical cues locally limit ring-directed cell cortex-
345 pulling at the lagging cell cortex (Figure 8G; arrows from the yellow boxes), thereby
346 suppressing the ring-directed cortical flow. The local suppression of the ring-directed
347 cortical flow should reduce compression-dependent myosin enrichment, resulting in the
348 formation of the structurally asymmetric ring observed in previous studies [6]. The local
349 reduction in myosin levels should then locally slow down ring edge advancement,
350 resulting in asymmetric ring closure.

351 Our analysis underscores the central role of the cortical flow pathway in ring
352 mechanosensation. Conversely, the RhoA pathway likely inhibits the mechanosensation
353 process. We found that reduced activities of the RhoA activator NOP-1 and effector LET-
354 502 did not influence ring eccentricity. However, we showed impaired
355 mechanosensitivity in *ani-1(RNAi)* embryos, in which myosin was highly enriched in the
356 contractile ring (Figure 8). Recent research has shown that ANI-1-binding proteins GCK-
357 1 and CCM-3 negatively regulate RhoA activity by promoting RhoGAP cortical

358 localization [47]. Therefore, it is likely that ANI-1 knockdown lifted this negative
359 regulation, leading to the activation of RhoA-dependent myosin enrichment. Indeed,
360 normal myosin enrichment as well as ring mechanosensitivity were restored in *ani-1;*
361 *nop-1* (Figure 8A–C). We propose that the balance between RhoA-dependent and cortical
362 flow-dependent myosin enrichment tunes ring mechanosensitivity (Figure 8H). The
363 mechanosensitivity of the ring should decrease when the contribution of the cortical flow
364 pathway-dependent myosin enrichment is negligible compared to that of RhoA-
365 dependent pathway (Figure 8H).

366 The structural asymmetry of the contractile ring in the *C. elegans* zygote likely
367 arises from asymmetric activity in the cortical flow-dependent feedback mechanisms
368 between the leading and lagging cell cortices [37]. A similar structural asymmetry has been
369 reported in *Drosophila* pupal dorsal thorax epithelia [11]. However, *Drosophila* embryonic
370 epithelial cells [2], follicular epithelia [34], and pupal wing epithelia [11] do not display such
371 structural asymmetry. As our study identified that the cortical flow-dependent feedback
372 mechanism mediates ring mechanosensation, this variability suggests that the
373 mechanosensitivity of contractile ring can be tuned differently during development,
374 enabling tissue-specific morphogenic cytokinesis. The cortical flow pathway likely
375 translates subtle differences in tissue mechanics into asymmetry in the furrowing rate,
376 while excessive RhoA activity could suppress ring-dependent mechanosensing. Cell
377 types that lack structurally asymmetric rings may undergo asymmetry ring closure by
378 relying on extreme differences in tissue stiffness (e.g., a stiffer apical cortex connected to
379 adherens junction vs a softer basal cortex) rather than on high ring mechanosensitivty.

380 Alternatively, these cell types might employ other mechanosensitive mechanisms, such as
381 mechanosensitive recruitment of myosin regulators to neighboring cells [48,49].
382 The tuning of ring mechanosensitivity would be critical in animal development.
383 Here, we will use lumen morphogenesis as an example to explain this concept. A
384 previous study showed that 3D cultures of epithelial cells initially undergo symmetric
385 cytokinesis to form a central lumen [12,50–53]. Subsequent ring closures are asymmetric,
386 maintaining a solitary lumen. In the case of intraflagellar transport protein IFT88
387 knockdown, the first cytokinesis becomes asymmetric, leading to the formation of
388 multiple lumens [12]. Consistently, a mouse model with a loss of function mutation of *ift88*
389 exhibits a polycystic kidney phenotype [54]. In this context, the contractile ring in the first
390 cytokinesis should exhibit lower mechanosensitivity to prevent ectopic unilateral
391 cytokinesis, while the contractile ring in subsequent cytokinesis should be highly
392 mechanosensitive. Our study provides a theoretical framework for a deeper
393 understanding of tissue-specific mechanochemical regulation of the contractile ring,
394 which is crucial for further elucidating the role of cytokinesis in these morphogenetic
395 events.
396

397 **Acknowledgements**

398 We thank Kota Mizumoto and Don Moerman for critical reading of the manuscript. Some
399 strains used in this study were obtained from the *Caenorhabditis* Genetics Center (funded
400 by the NIH Office of Research Infrastructure Programs; P40 OD010440). We also thank
401 Bruce Bowerman for providing valuable advice, Chris Doe for sharing lab equipment,
402 and the Sugioka lab members for general discussions. This work was supported by the

Canadian Institutes of Health Research (Project Grant; PJT-169145), Government of Canada's New Frontiers in Research Fund (NFRFE-2019-00310), and the Health Research BC (Scholar Award; SCH-2020-0406) to K.S. C.R.H was supported by British Columbia Graduate Scholarship.

Author contributions

C.R.H.: Formal analysis, Investigation, Writing-Original Draft, Validation, Visualization. **G.S.**: Formal analysis, Investigation, Validation, Visualization. **W.F.**: Formal analysis, Investigation. **J.Z.**: Formal analysis, Investigation. **K.S.**: Conceptualization, Formal analysis, Investigation, Methodology, Software, Validation, Writing-Original Draft, Writing-Review & Editing, Supervision, Funding acquisition.

Declaration of interests

The authors declare no competing interests.

421 # Methods

422 **Experimental Model and Subject Details**

423 All *C. elegans* strains were cultured using the standard method [55]. A temperature
424 sensitive-actin mutant *act-2(or295)* was cultured at 15 ºC until the L4 larval stage and
425 incubated at 25 ºC overnight before imaging. The following transgenes were used:
426 *cp13*[*nmy-2*::GFP + LoxP] (non-muscle myosin II) [56], *or1940*[GFP::*sas-7*] (centriole
427 marker) [57], *itIs37* (mCherry::histone H2B), *ruIs32*[*pie*-1p::GFP::H2B::*pie-1* 3'UTR +
428 *unc-119*(+)].

429

430 **RNAi**

431 Feeding RNAi was performed at 25 ºC using the standard method [58]. For control RNAi, a
432 bacterial strain carrying an empty vector (L4440) was used. To observe *let-502(RNAi)* P_0
433 zygotes, the L2 stage larvae were cultured on freshly prepared feeding RNAi plates on
434 day 1. The L4 larvae were then transferred to new feeding RNAi plates on day 2 and
435 imaged on day 3. For observing *let-502(RNAi)* AB cell, we performed L4 RNAi to avoid
436 abnormal AB spindle orientation. For *pod-1* and *mlc-4*, L4 larvae were cultured on
437 feeding RNAi plates and used for imaging on the next day.

438

439 **Blastomere isolation**

440 Blastomeres were isolated as described before [59], with some modification [60]. We cut the
441 gravid adult worms in egg salt buffer and treated them with hypochlorite solution [75%
442 Clorox (Clorox) and 2.5N KOH] for 50 s. After washing twice with Shelton's growth
443 medium [61], embryos were transferred to fresh Shelton's growth medium. Eggshell and

444 permeability barrier were removed by mouth pipetting with hand-drawn microcapillary
445 tubes (10 µL, Kimble Glass Inc.). The two-cell stage eggshell-free embryos were further
446 pipetted to remove the cell-cell contact.
447
448 **Adhesive polystyrene bead preparation**
449 The detailed method is described in our previous papers [1,60]. Approximately 10 mg
450 carboxyl-modified polystyrene beads with diameters of 30 µm (Kisker Biotech GmbH &
451 Co.), 20 µm, 10 µm, and 4.5 µm (Polysciences) were washed twice with 100 mM 2-(N-
452 morpholino) ethanesulfonic acid (MES) buffer (pH6.5) and incubated with 1 mL MES
453 buffer containing 10 mg 1-Ethyl-3-(3-dimethylaminopropyl) carbodiimide (EDAC) for
454 15 min at room temperature (22.5˚C). We washed the beads twice with phosphate-
455 buffered saline (PBS) and incubated them with 0.5 mL PBS containing 0.05 µg
456 Rhodamine Red-X succinimidyl ester (ThermoFisher Scientific) for 5 min. The
457 appropriate concentration was also determined by treating the beads with a series of
458 serially diluted Rhodamine Red-X solution [60]. The beads were washed twice with PBS
459 and stored in PBS at 4 ºC. Adhesiveness of the beads was confirmed by attaching them to
460 the isolated blastomere using the mouth pipette. If successful, the adhesion is firmly
461 established and cells do not dissociate spontaneously.
462
463 **Live-imaging sample preparation**
464 To obtain embryos, gravid adults were dissected on a coverslip, in a droplet of 10–12 µl
465 of refractive index-matching medium (30% iodixanol diluted in egg salt buffer,
466 supplemented with 30 µm diameter plain polystyrene beads) as described before [42]. After

467 placing the coverslip gently onto a slide glass, three edges of coverslip were sealed with
468 petroleum jelly (Vaseline), with one edge remaining open to the air. We realized that this
469 method improved the success rate of imaging for inexperienced users. Inexperienced
470 users may observe cell death due to the acute compression during the sample preparation
471 and require training using control strains. If all the processes were performed correctly,
472 the imaging condition does not have adverse effects on the embryonic viability, as judged
473 by normal cell division in the next cell cycle.
474
475 **Microscopy**
476 Intact embryos were imaged using a microscope Olympus IX83 (Olympus), equipped
477 with a spinning-disk confocal unit CSU-W1 (Yokogawa), a scientific CMOS camera
478 Prime 95B (Photometrics), a piezoelectric stage NANO-Z (Mad City Labs), a silicon
479 immersion objective UPLSAPO60XS2 (NA1.3, 60X; Olympus), and a beam splitter
480 Optosplit II (Cairn Research), which is controlled by Cellsense Dimension (Olympus). A
481 silicone immersion oil (Z81114; refractive index: 1.406 at 23 ºC; Olympus) was used as
482 an immersion medium. Samples were illuminated by diode-pumped lasers with 488 nm
483 and 561 nm wavelengths, and the simultaneous two color-imaging was performed with
484 150 ms camera exposure time, 1 μm Z-step size with a total of 31 slices per frame, 5.6-s
485 interval, and the duration of 15 min. Isolated blastomeres were imaged using a
486 microscope Leica DMi8 (Leica Microsystems), equipped with a spinning-disk confocal
487 unit CSU-W1 with Borealis (Andor Technology), dual EMCCD cameras iXon Ultra 897
488 (Andor Technology), and an oil-immersion PL APO objective lens (NA1.4, 63X; Leica),
489 and controlled by Metamorph (Molecular Devices). Data in Figure 7B and 7F were

490 imaged with 1.5 µm Z-step size and 15-s intervals. Data in Figure 7D were imaged with
491 1.5 µm Z-step size and 10-s intervals, with only the half volume closer to the objective
492 lens imaged.
493
494 **Quantification of the P_0 contractile ring dynamics**
495 The obtained 4D data were deconvoluted using a constrained iterative and advanced
496 maximum likelihood algorithm (iteration: 5), using Olympus Cellsens software
497 (Olympus, Inc). Each 4D tiff stack file was processed using Fiji [62] (Figure S1). The
498 deconvoluted images were processed using Gaussian blur (sigma = 2) and an image J
499 plug-in "attenuation correction" (opening =3, reference =15) [63]. A 10-µm W x 32 µm H
500 boxed region corresponding to the contractile ring was selected and adjusted for the
501 fluorescence intensity so that the signal would not be saturated in the next step, and
502 rotated by 3D projection (Brightest point, interpolation on). After selecting a plane of en
503 face ring view, the images were segmented and quantified using an Image J plug-in
504 Morpholib J [64]. The segmented contractile ring areas were measured for ring radius, ring
505 centroid, and ring angle. The radius of the segmented area was estimated using ellipsoid
506 fitting and derived by calculating the average of major and minor radii of the ellipsoid.
507 Data were aligned relative to the time point first exceeded 10% ring closure. The ring
508 trajectory images were obtained with an in-house image J macro using same data.
509
510 **Quantification of the intact AB contractile ring dynamics**
511 Since the AB cell undergoes rotation during its division, the precise quantification is
512 challenging. We first selected samples undergoing unilateral cleavage roughly in parallel

513 to the imaging plane, and corrected for cell rotation using Stackreg plug-in of Image J [65],
514 using chromosome signal (polar bodies were deleted using a brush tool to avoid abnormal
515 image registration) (Figure S5). The rotation-corrected images were then processed by
516 the same pipeline used for the P_0 cell.
517
518 **3D visualization and quantification of contractile ring dynamics in isolated**
519 **blastomeres**
520 The oblique view of cells in Figures 1A, 7A–B, and 7F were generated using an Image J
521 plug-in Clear Volume [66]. The analysis of the contractile ring dynamics in isolated
522 blastomeres is challenging since the cell is rotated along different axes, and not all the
523 planes were captured during imaging. Thus, we made en face ring view images for each
524 time point using Clear Volume, and estimated the cell and ring contours, centroids, and
525 diameters, by selecting more than four points along the cell and ring perimeter,
526 respectively, using an Image J macro "Smallest Enclosing Circle" [62]. The ring closure
527 rate and eccentricity were calculated using the method described above for other cells.
528 Measurements were performed three times per sample, and average values were used to
529 mitigate the relatively higher error rate compared to the automatic segmentation method
530 used for intact embryos.
531
532 **Kymographs**
533 Kymographs in Figure 4D were generated by stacking 1 μm H x 40 μm W rectangular
534 regions at a given time. Kymographs in Figure 4E were generated by stacking 11 μm W x
535 3.7 μm H rectangular regions corresponding to a myosin cluster. The timing is adjusted

536 so that the peak myosin cluster intensity comes fourth out of a total of eight frames, using
537 an in-house image J macro.
538
539 **Quantification of myosin enrichment rate**
540 We measured myosin enrichment using the ring en face view of NMY-2::GFP, as shown
541 in Figure 8B. Selection of the contractile ring region was performed using the
542 segmentation data described above. However, unlike the highly pre-processed data used
543 for segmentation (e.g., attenuation corrected), we used raw myosin data without
544 deconvolution and other processes. The only processes performed were 3D projection
545 and interpolation. After binarizing the segmentation data, we dilated the mask four times
546 (mask 1) and also created another mask with four times erosion (mask 2). In our
547 condition, mask1 covered most of the ring area, while mask 2 covered the area inside the
548 ring (cytoplasm). The myosin signal at each time point was then quantified by subtracting
549 the signal in mask 2 from the signal in mask 1. The timing of these time series data was
550 aligned relative to 10% ring closure.
551
552 **Particle Image Velocimetry**
553 A detailed image preprocessing pipeline is shown in Figure S3. Briefly, 4D data sets of
554 NMY-2::GFP and GFP::-SAS-7-expressing embryos were processed with Gaussian Blur
555 (sigma =1) and unsharp mask (radius =1, mask = 0.6) using Fiji. Centriole signals were
556 deleted by filling zero values. After intensity adjustment to avoid signal saturation, half
557 volume of image stack was filled with zero values to avoid projecting cortical myosin
558 from opposite cortical sides. The images obtained were projected using an Image J

559 function "3D projection." We rotated 3D projected data relative to angle of cleavage at
560 25% closure and generated leading and lagging cortex views. Note that not always both
561 lagging and leading cortices were clearly visible, so that in some embryos, either the
562 leading or lagging cortex was used. Using these flattened cell cortex images, Particle
563 Image Velocimetry was performed using MATLAB software PIV LAB (Algorithm: FFT
564 window deformation, Interrogation area: 5.8 µm, Step size: 2.9 µm, Sub-pixel estimator:
565 Gauss 2x3 point, Correlation robustness: Standard) [43]. We rejected vectors exceeding
566 0.25 µm/s to remove estimation errors (the setting was visually confirmed to reflect the
567 myosin foci movement). Obtained 3D matrix data (2D x time) were used for downstream
568 analyses. The PIV matrix data were aligned relative to 10% ring closure, centered relative
569 to the cell center corresponding to the furrow position, and resized to contain an entire
570 embryo using Numpy and Pandas [67,68].
571

572 **Estimation of cortical convergence**

573 Cortical convergence was derived using the PIV vector matrix and a NumPy gradient
574 function [67]. When we define A-P-axis and circumferential-axis cortical flow velocities in
575 an i x j matrix as $u_{i,j}$ and $v_{i,j}$, respectively, $u_{i+h,j}$, $u_{i-h,j}$, $v_{i,j+h}$, $v_{i,j-h}$ can be defined as
576 follows using Taylor series [69]:

577 $$u_{i+h,j} = u_{i,j} + h\frac{\partial u_{i,j}}{\partial i} + \frac{h^2}{2!}\frac{\partial^2 u_{i,j}}{\partial i^2} + \mathcal{O}(h^3) \qquad (4)$$

578 $$u_{i-h,j} = u_{i,j} - h\frac{\partial u_{i,j}}{\partial i} + \frac{h^2}{2!}\frac{\partial^2 u_{i,j}}{\partial i^2} + \mathcal{O}(h^3) \qquad (5)$$

579 $$v_{i,j+h} = v_{i,j} + h\frac{\partial v_{i,j}}{\partial j} + \frac{h^2}{2!}\frac{\partial^2 v_{i,j}}{\partial j^2} + \mathcal{O}(h^3) \qquad (6)$$

$$v_{i,j-h} = v_{i,j} - h\frac{\partial v_{i,j}}{\partial j} + \frac{h^2}{2!}\frac{\partial^2 v_{i,j}}{\partial j^2} + \mathcal{O}(h^3) \quad (7)$$

And we will obtain the following by subtraction:

$$u_{i+h,j} - u_{i-h,j} = 2h\frac{\partial u_{i,j}}{\partial i} + \mathcal{O}(h^3) \quad (8)$$

$$V_{i,j+h} - V_{i,j-h} = 2h\frac{\partial v_{i,j}}{\partial j} + \mathcal{O}(h^3) \quad (9)$$

Thus, the cortical flow gradients at the interior points can be defined as follows:

$$\frac{\partial u_{i,j}}{\partial i} = \frac{u_{i+h,j} - u_{i-h,j}}{2h} + \mathcal{O}(h^2) \approx \frac{u_{i+h,j} - u_{i-h,j}}{2h} \quad (10)$$

$$\frac{\partial V_{i,j}}{\partial j} = \frac{v_{i,j+h} - v_{i,j-h}}{2h} + \mathcal{O}(h^2) \approx \frac{v_{i,j+h} - v_{i,j-h}}{2h} \quad (11)$$

At the boundary, first order one-sided differences were achieved as follows:

$$\frac{\partial u_{i,j}}{\partial i} = \frac{u_{i+h,j} - u_{i,j}}{h} + \mathcal{O}(h) \approx \frac{u_{i+h,j} - u_{i,j}}{h} \quad (12)$$

$$\frac{\partial v_{i,j}}{\partial j} = \frac{v_{i,j+h} - v_{i,j}}{h} + \mathcal{O}(h) \approx \frac{v_{i,j+h} - v_{i,j}}{h} \quad (13)$$

A-P-axis and circumferential-axis cortical convergence $p_{i,j}$, and $q_{i,j}$, respectively, were calculated as follows, where *a* is the PIV step size:

$$p_{i,j} = -\frac{1}{a}\frac{\partial u_{i,j}}{\partial i} \approx -\frac{1}{a}\frac{\left(u_{i+1,j} - u_{i-1,j}\right)}{2} \quad (at\ the\ interior\ points)\ (14)$$

$$p_{i,j} = -\frac{1}{a}\frac{\partial u_{i,j}}{\partial i} \approx -\frac{1}{a}\left(u_{i\pm1,j} - u_{i,j}\right) \quad (at\ the\ boundary) \quad (15)$$

$$q_{i,j} = -\frac{1}{a}\frac{\partial v_{i,j}}{\partial j} \approx -\frac{1}{a}\frac{\left(v_{i,j+1} - v_{i,j-1}\right)}{2} \quad (at\ the\ interior\ points)\ (16)$$

$$q_{i,j} = -\frac{1}{a}\frac{\partial v_{i,j}}{\partial j} \approx -\frac{1}{a}\left(v_{i,j\pm1} - v_{i,j}\right) \quad (at\ the\ boundary) \quad (17)$$

596 To quantify leading and lagging cortex convergence at the equatorial region, we
597 calculated the mean convergence within a 6x3 grid (14.6 μm W x 5.9 μm H) around the
598 center of the furrow position.
599
600 **Myosin foci tracking**
601 Myosin foci were tracked using Manual Tracking plug-in of Image J.
602 In Figure 7D–E, cell position was registered using image J plug-in Stackreg, to eliminate
603 the movement of myosin foci caused by the movement of cell body.
604
605 **Statistical analysis**
606 For multiple comparisons, one-way ANOVA with the Holm–Sidak's method was used.
607 The comparison of two data was performed using the Welch's t-test. No statistical
608 method was used to predetermine the sample size. Error bars or bands correspond to the
609 95% confidence interval. The experiments were not randomized. The investigators were
610 not blinded to the study. Statistical analyses were performed using either SciPy or Prism
611 9 (Graphpad). Symbols such as "****," "***," "**," and "*" indicate $p < 0.0001$, $p <$
612 0.001, $p < 0.01$, and $p < 0.05$, respectively.
613

614 ## Data availability

615 The data used in this study is available in the Source Data file.

616 ## Code availability

617 The codes used in this study are available at
618 https://github.com/sugi01/unilateralcytokinesis.

619 **Figure legends**

620

621 **Figure 1. Quantitative analysis of asymmetric contractile ring closure in the *C.***
622 ***elegans* zygote.**

623 (**A**) Asymmetric contractile ring closure in *C. elegans* zygote. NMY-2::GFP (green, non-
624 muscle myosin II), GFP::SAS-7 (green, centriole) and histone H2B::mCherry (magenta,
625 chromosome) are shown. In this and subsequent figures, anterior and posterior are to the
626 left and right, respectively. (**B**) Computationally reconstructed ring and segmentation
627 results. The top left image shows cytokinesis onset, and the second and third rows
628 highlight the advancement of the leading and lagging ring edges, respectively. See Fig S1
629 for method and full frame images. (**C**) Trajectory of ring constriction. Outlines of the
630 contractile ring during cytokinesis are plotted based on the segmentation results. The
631 color coding indicates time relative to cytokinesis onset. (**D**) Geometric analysis of the
632 contractile ring closure. Eccentricity and ring edge advancement are the degree of ring
633 off-centering and the distance between the ring edge and initial ring perimeter,
634 respectively. (**E**) Mean ring closure and eccentricity. (**F**) Mean ring edge advancement.
635 Lagging furrowing onset was defined as the timing when the $L_{lag}(t)$ exceeded 0.02 (2%
636 relative to initial ring size). (**G**) Definitions of time lag and ring closure velocity (See
637 text). Times are relative to cytokinesis onset. Error bands indicate 95% confidence
638 intervals. Scale bars, 10 μm.

639

640 **Figure 2. Ring closure velocity and a delay in lagging edge furrowing collectively**
641 **determine the ring eccentricity.**

642 (**A**) Relationship between peak eccentricity, ring closure velocity, and time lag in normal
643 cells. (**B**) Relationship between peak eccentricity and normalized time lag in normal cells.
644 (**C**) Ring trajectories of different RNAi and mutant backgrounds. (**D**) Peak eccentricity
645 and normalized time lag in different backgrounds. (**E**) Relationship between peak
646 eccentricity and normalized time lag in different backgrounds. (**F**) The relationship
647 between ring closure velocity and time lag in different backgrounds. (**G**) Time lag and
648 ring closure velocity. Times are relative to cytokinesis onset. Error bars indicate 95%
649 confidence intervals except for panel E and F, in which standard deviations were shown.
650 The value r represents Pearson's correlation coefficient. *P*-values were calculated using
651 one-way ANOVA followed by Holm–Sidak's multiple comparison test. Scale bars, 10
652 μm.
653
654 **Figure 3. Reduced ring-directed cortical flow at the lagging cell cortex accompanies**
655 **circumferential-axis cortical flow.**
656 (**A**) A cortical flow-dependent positive feedback model in the contractile ring assembly.
657 Ring-dependent cell cortex pulling generates ring-directed cortical flow and induces ring-
658 directed compression. Resulting myosin enrichment to the ring further facilitates ring
659 constriction. (**B**) Measurement of cortical flow. Leading and lagging cortex views were
660 generated by computationally rotating 4D timelapse data. Cortical flow vectors were
661 estimated using particle image velocimetry (yellow arrows). Convergence of cortical
662 flow vectors were calculated to estimate the influx of cortical flow within the equatorial
663 ROI (black boxes). (**C**) The relationship between ring edge advancement and ring-
664 directed cortical flow. Cortical flow in the area anterior to the ring is shown. (**D**) A-P axis

665 convergence and circumferential axis convergence in leading and lagging cell cortices.
666 (**E**) Myosin foci tracking during cytokinesis. Scale bars, 10 μm.
667
668 **Figure 4. Cells undergoing asymmetric ring closure exhibit polarized mechanical**
669 **loading at the lagging cortex.**
670 (**A**) Inferring cortical mechanics from cortical convergence data. Before furrowing onset,
671 cortical convergence is proportional to the cortical compression. After furrowing onset,
672 convergence is proportional to the sum of compression and invagination. (**B**) Cortical
673 compression at the lagging equatorial cell cortex. Mean cortical flow convergence before
674 the onset of lagging edge furrowing is shown. The transparent parts of graphs show the
675 convergence after the furrowing onset. Red and blue arrowheads indicate local maxima
676 and minima between cytokinesis onset (left dotted line) and lagging edge furrowing onset
677 (right dotted line) in each graph. (**C**) Reduction rate of ring-directed compression at the
678 lagging equatorial cortex. (**D**) Peak circumferential axis convergence observed at the
679 lagging equatorial cortex. (**E**) Relationship between peak circumferential axis
680 convergence and ring closure velocity. The value r represents Pearson's correlation
681 coefficient. (**F**) Summary of the cortical flow and cortical compression at the lagging
682 equatorial cell cortex. Ring-directed compression decreases as the circumferential
683 compression increases. P-values were calculated using one-way ANOVA followed by
684 Holm-Sidak's multiple comparison test. Times are relative to cytokinesis onset. Error
685 bands and bars indicate 95% confidence intervals. Scale bars, 10 μm.
686

687 **Figure 5. Non-ring-directed cortical compression suppresses ring-directed cortical**
688 **flow.**
689 (**A**) Kymographs of cortical myosin. Yellow boxes in the top images were used to
690 generate kymographs. (**B**) Ring-directed cortical flow in control zygotes. Leading edge
691 shows consistent flow while the lagging edge flow is preceded by the stabilization. (**C**)
692 Ring-directed cortical flow in *act-2* mutant zygotes. A myosin focus movement during
693 contraction and relaxation of the area behind the ring was shown. (**D**) Averaged ring-
694 directed flow in *act-2* mutant zygotes. (**E**) The mechanism of compression-dependent
695 suppression of the ring-directed cortical flow. While ring-directed compression promotes
696 ring assembly, non-ring-directed compression suppresses ring-directed cortical flow.
697 Times are relative to cytokinesis onset. Scale bars, 10 μm.
698
699 **Figure 6. Non-ring-directed cortical compression delays ring edge advancement**
700 **without suppressing ring constriction.**
701 (**A**) Contractile ring trajectory of a single *act-2(or295ts)* mutant (left panel) and the mean
702 values of ring closure and eccentricity (graph). (**B**) Planes shown in (C–E). Changes in
703 myosin intensity indicate contraction and relaxation. (**C**) NMY-2::GFP at the top surface
704 during cytokinesis. Yellow and light blue dotted circles indicate the area exhibiting
705 contraction and relaxation, respectively. (**D**) Ring en face view of the same embryo
706 shown in panel C. Dotted lines indicate top and bottom limits of the contractile ring.
707 Arrows indicate the movement of the ring limit. (**E**) Ring trajectories of the contractile
708 ring shown in (D). Top- and bottom-oriented movements are shown in yellow and blue,
709 respectively. (**F**) Relationship between top ring acceleration and myosin intensity

710 changes. Positive ring edge acceleration represents ring ingression toward the bottom
711 surface. (**G**) Top ring edge acceleration upon contraction and relaxation. (**H**) Top ring
712 edge acceleration measured 5.6 s post-contraction and relaxation. (**I**) Ring center
713 acceleration 5.6 s after contraction and relaxation. Error bars and bands indicate 95%
714 confidence intervals. Scale bars, 10 μm.
715
716 **Figure 7. Artificial inhibition of ring-directed cortical flow is sufficient to induce**
717 **asymmetric ring closure.**
718 (**A**, **B**) Contractile ring closure in the intact and isolated AB cell. NMY-2::GFP and
719 mCherry::histone H2B (left), ring trajectories (middle), and ring closure and eccentricity
720 curves (right) are shown. (**C**) Mean peak eccentricity of the contractile ring in the AB
721 cells. (**D**, **E**) Attachment of different sized adhesive beads to the isolated AB cell. Ring-
722 directed cortical flow were plotted for proximal and distal to the bead attachment site in
723 E. (**F**–**H**) Oblique view of contractile rings in the bead attached AB cell. Ring trajectory
724 and mean eccentricity are shown in G and H, respectively. Times are relative to
725 cytokinesis onset. Error bands and bars indicate 95% confidence intervals. Scale bars, 10
726 μm.
727
728 **Figure 8. Anillin tunes contractile ring mechanosensitivity.**
729 (**A**) Heatmaps of peak eccentricity and peak circumferential-axis convergence. *ani-*
730 *1(RNAi)* embryos exhibit defects in asymmetric ring closure in both P_0 and AB cells. (**B**,
731 **C**) Contractile ring myosin enrichment. Total myosin signal intensity in the ring (B) was
732 used to estimate myosin enrichment rate in (C). (**D**-**F**) Relationship among ring closure

733 velocity, peak ring-directed cortical flow, and myosin enrichment rate. (**G**) Proposed
734 model of contractile ring-dependent mechanosensation. (**H**) Proposed model of Anillin-
735 dependent tuning of contractile ring mechanosensitivity. Error bars indicate 95%
736 confidence intervals. Scale bars, 10 µm. p-values were calculated by one-way ANOVA
737 with Holm-Sidak's multiple comparison test.
738
739 **Figure S1. Imaging and contractile ring analysis methods of P_0 zygotes.**
740 (**A**) Imaging conditions and analytical flow charts. We used refractive index matching
741 medium and polystyrene beads to prevent light scattering and cellular compression. The
742 use of a refractive index matching medium reduced the required slice number from 34 to
743 31 and also improved image resolution, especially on the deeper side of the cell (focal
744 planes far from the objective lens). (**B**) Temporal color-coded image of 20 frames around
745 cytokinesis onset showing that compression-free embryos do not exhibit global cortical
746 rotation. (**C**) Ring en face view images of 3D projected data and segmentation results.
747 The first and last frames are the top left and bottom right in these figures, respectively.
748 (**D**) Contractile ring closure curve after alignment of time series data relative to 10 %
749 ring closure. Error bars indicate 95% confidence intervals. As we also measured myosin
750 signal intensity and cortical flow dynamics using the same data set, all the data were
751 aligned using the time relative to cytokinesis onset (or normalized time relative to
752 cytokinesis onset) unless otherwise specified.
753
754 **Figure S2. Ring closure dynamics in RNAi and mutant backgrounds tested in this**
755 **study.**

756 (**A**-**F**) Ring closure, Eccentricity, and Ring edge advancement curves were plotted against
757 time relative to cytokinesis onset. See Figure S3 for the data plotted against normalized
758 time. Lagging furrowing onset was defined as the time when the $L_{lag}(t)$ exceeded 0.02
759 (2% relative to initial ring size). (**G**) Relationship between peak eccentricity and time lag
760 (raw values without normalization).
761
762 **Figure S3. Generation of cortical myosin data used for Particle Image Velocimetry**
763 **(PIV) analysis.**
764 (**A**) An image preprocessing pipeline used to generate cortical myosin data for PIV
765 analyses. See also Methods section. During the quality control step, very noisy or dim
766 images were excluded from PIV analyses. These images are usually from image planes
767 furthest from the objective lens.
768
769 **Figure S4. Cortical convergence in *let-502(RNAi)* and *pod-1(RNAi)*.**
770 (**A**) A-P axis and circumferential axis convergece curves plotted against actual time (in
771 seconds)
772
773 **Figure S5. Imaging and contractile ring analysis methods of the two-cell stage AB**
774 **cell.**
775 (**A**) Imaging conditions and analytical flow charts. Intact AB cells were analyzed similar
776 to the P0 cells with some modifications to correct for cellular rotation. For isolated AB
777 blastomeres, we used normal growth medium and a different analytical pipeline to

778 estimate ring size and position due to the movement and rotation of the cells. Isolated AB
779 cells were measured three times, and average values were analyzed.
780
781 **Movie S1. Dynamics of cortical myosin and contractile ring of a single embryo**
782 Left top: maximum projection of cell surface NMY-2::GFP. Bottom left: ring en face
783 view of NMY-2::GFP. Bottom middle: segmented ring. Bottom right: reconstructed ring
784 trajectory. Right graph: Contractile ring dynamics of the same embryo. Note that the
785 same embryo was used to generate all data.
786
787 **Movie S2. Cortical flow and flow vector map using Particle Image Velocimetry**
788 The cell surface NMY-2::GFP of leading (left), lateral (middle), and lagging cortex views
789 (right). Yellow arrows are generated by Particle Image Velocimetry. Times are relative to
790 cytokinesis onset.
791
792 **Movie S3. Dynamics of cortical compression and cortical ingression in *act-2(or295)***
793 Cell surface (top) and ring en face view (bottom left) of NMY-2::GFP. Ring outlines and
794 centroid trajectory were color-coded as in Figure 6E (yellow: movement towards the the
795 contraction site, blue: movement away from the relaxation site).
796
797
798
799
800

801 **References**

802 1. Sugioka, K. & Bowerman, B. Combinatorial Contact Cues Specify Cell Division
803 Orientation by Directing Cortical Myosin Flows. *Dev. Cell* **46**, 257-270.e5 (2018).
804 2. Guillot, C. & Lecuit, T. Adhesion disengagement uncouples intrinsic and extrinsic
805 forces to drive cytokinesis in epithelial tissues. *Dev. Cell* **24**, 227–241 (2013).
806 3. Pham, T. T. *et al.* Spatiotemporally Controlled Myosin Relocalization and Internal
807 Pressure Generate Sibling Cell Size Asymmetry. *iScience* **13**, 9–19 (2019).
808 4. Thieleke-Matos, C., Osório, D. S., Carvalho, A. X. & Morais-de-Sá, E. Emerging
809 Mechanisms and Roles for Asymmetric Cytokinesis. *Int. Rev. Cell Mol. Biol.* **332**,
810 297–345 (2017).
811 5. Rappaport, R. Division Mechanism Function and Its Consequences. in *Cytokinesis*
812 *in Animal Cells* 230–264 (Cambridge University Press, 1996).
813 6. Maddox, A. S., Lewellyn, L., Desai, A. & Oegema, K. Anillin and the septins
814 promote asymmetric ingression of the cytokinetic furrow. *Dev. Cell* **12**, 827–835
815 (2007).
816 7. Ferguson, D. J. P. An ultrastructural study of mitosis and cytokinesis in normal
817 'resting' human breast. *Cell Tissue Res.* **252**, 581–587 (1988).
818 8. Jinguji, Y. & Ishikawa, H. Electron microscopic observations on the maintenance of
819 the tight junction during cell division in the epithelium of the mouse small intestine.
820 *Cell Struct. Funct.* **17**, 27–37 (1992).
821 9. Vogetseder, A., Karadeniz, A., Kaissling, B. & Le Hir, M. Tubular cell proliferation
822 in the healthy rat kidney. *Histochem. Cell Biol.* **124**, 97–104 (2005).

10. Ziegler, H. E. Experimentelle studien über zelltheilung. IV. Die zelltheilung der furchungzellen bei Beroe und Echinus. *Archiv für Entwicklungsmechanik der Organismen* **16**, 155–175 (1903).

11. Herszterg, S., Leibfried, A., Bosveld, F., Martin, C. & Bellaiche, Y. Interplay between the Dividing Cell and Its Neighbors Regulates Adherens Junction Formation during Cytokinesis in Epithelial Tissue. *Dev. Cell* **24**, 256–270 (2013).

12. Taulet, N. *et al.* IFT proteins spatially control the geometry of cleavage furrow ingression and lumen positioning. *Nat. Commun.* **8**, 1928 (2017).

13. Gómez-Cavazos, J. S. *et al.* A Non-canonical BRCT-Phosphopeptide Recognition Mechanism Underlies RhoA Activation in Cytokinesis. *Curr. Biol.* **30**, 3101-3115.e11 (2020).

14. Somers, W. G. & Saint, R. A RhoGEF and Rho family GTPase-activating protein complex links the contractile ring to cortical microtubules at the onset of cytokinesis. *Dev. Cell* **4**, 29–39 (2003).

15. Tatsumoto, T., Xie, X., Blumenthal, R., Okamoto, I. & Miki, T. Human ECT2 is an exchange factor for Rho GTPases, phosphorylated in G2/M phases, and involved in cytokinesis. *J. Cell Biol.* **147**, 921–928 (1999).

16. Yüce, O., Piekny, A. & Glotzer, M. An ECT2-centralspindlin complex regulates the localization and function of RhoA. *J. Cell Biol.* **170**, 571–82 (2005).

17. Matsumura, F. Regulation of myosin II during cytokinesis in higher eukaryotes. *Trends Cell Biol.* **15**, 371–377 (2005).

844 18. Otomo, T., Otomo, C., Tomchick, D. R., Machius, M. & Rosen, M. K. Structural
845 basis of Rho GTPase-mediated activation of the formin mDia1. *Mol. Cell* **18**, 273–
846 281 (2005).
847 19. Basant, A. & Glotzer, M. Spatiotemporal Regulation of RhoA during Cytokinesis.
848 *Curr. Biol.* **28**, R570–R580 (2018).
849 20. Chapa-Y-Lazo, B., Hamanaka, M., Wray, A., Balasubramanian, M. K. & Mishima,
850 M. Polar relaxation by dynein-mediated removal of cortical myosin II. *J. Cell Biol.*
851 **219**, (2020).
852 21. Wolpert, L. The mechanics and mechanism of cleavage. *Int. Rev. Cytol.* **10**, 163–
853 216 (1960).
854 22. von Dassow, G., Verbrugghe, K. J. C., Miller, A. L., Sider, J. R. & Bement, W. M.
855 Action at a distance during cytokinesis. *J. Cell Biol.* **187**, 831–845 (2009).
856 23. Werner, M., Munro, E. & Glotzer, M. Astral signals spatially bias cortical myosin
857 recruitment to break symmetry and promote cytokinesis. *Curr. Biol.* **17**, 1286–1297
858 (2007).
859 24. Mangal, S. *et al.* TPXL-1 activates Aurora A to clear contractile ring components
860 from the polar cortex during cytokinesis. *J. Cell Biol.* **217**, 837–848 (2018).
861 25. Chen, A. *et al.* Inhibition of polar actin assembly by astral microtubules is required
862 for cytokinesis. *Nat. Commun.* **12**, 2409 (2021).
863 26. Rodrigues, N. T. L. *et al.* Kinetochore-localized PP1-Sds22 couples chromosome
864 segregation to polar relaxation. *Nature* **524**, 489–492 (2015).
865 27. Kiyomitsu, T. & Cheeseman, I. M. Cortical dynein and asymmetric membrane
866 elongation coordinately position the spindle in anaphase. *Cell* **154**, 391–402 (2013).

867 28. Yatsu, N. Observations and experiments on the ctenophore egg. *Jour. Coll. Sci.*
868 *Tokyo* **32**, 1–21 (1912).
869 29. Rappaport, R. & Conrad, G. W. AN EXPERIMENTAL ANALYSIS OF
870 UNILATERAL CLEAVAGE IN INVERTEBRATE EGGS. *J. Exp. Zool.* **153**, 99–
871 112 (1963).
872 30. Bement, W. M., Benink, H. A. & von Dassow, G. A microtubule-dependent zone of
873 active RhoA during cleavage plane specification. *J. Cell Biol.* **170**, 91–101 (2005).
874 31. Fleming, E. S. *et al.* Planar spindle orientation and asymmetric cytokinesis in the
875 mouse small intestine. *J. Histochem. Cytochem.* **55**, 1173–80 (2007).
876 32. Woolner, S. & Papalopulu, N. Spindle position in symmetric cell divisions during
877 epiboly is controlled by opposing and dynamic apicobasal forces. *Dev. Cell* **22**, 775–
878 787 (2012).
879 33. Nakajima, Y.-I. *et al.* Junctional tumor suppressors interact with 14-3-3 proteins to
880 control planar spindle alignment. *J. Cell Biol.* **218**, 1824–1838 (2019).
881 34. Morais-de-Sá, E. & Sunkel, C. Adherens junctions determine the apical position of
882 the midbody during follicular epithelial cell division. *EMBO Rep.* **14**, 696–703
883 (2013).
884 35. Tse, Y. C. *et al.* RhoA activation during polarization and cytokinesis of the early
885 Caenorhabditis elegans embryo is differentially dependent on NOP-1 and CYK-4.
886 *Mol. Biol. Cell* **23**, 4020–4031 (2012).
887 36. Founounou, N., Loyer, N. & Le Borgne, R. Septins regulate the contractility of the
888 actomyosin ring to enable adherens junction remodeling during cytokinesis of
889 epithelial cells. *Dev. Cell* **24**, 242–255 (2013).

890 37. Khaliullin, R. N. *et al.* A positive-feedback-based mechanism for constriction rate
891 acceleration during cytokinesis in Caenorhabditis elegans. *Elife* **7**, (2018).
892 38. Reymann, A.-C., Staniscia, F., Erzberger, A., Salbreux, G. & Grill, S. W. Cortical
893 flow aligns actin filaments to form a furrow. *Elife* **5**, e17807 (2016).
894 39. Li, Y. & Munro, E. Filament-guided filament assembly provides structural memory
895 of filament alignment during cytokinesis. *Dev. Cell* **56**, 2486-2500.e6 (2021).
896 40. Singh, D., Odedra, D., Dutta, P. & Pohl, C. Mechanical stress induces a scalable
897 switch in cortical flow polarization during cytokinesis. *J. Cell Sci.* **132**, (2019).
898 41. Schonegg, S., Hyman, A. A. & Wood, W. B. Timing and mechanism of the initial
899 cue establishing handed left–right asymmetry in Caenorhabditis elegans embryos.
900 *Genesis* **52**, 572–580 (2014).
901 42. Xiong, R. & Sugioka, K. Improved 3D cellular morphometry of Caenorhabditis
902 elegans embryos using a refractive index matching medium. *PLoS One* **15**,
903 e0238955 (2020).
904 43. Thielicke, W. & Sonntag, R. Particle Image Velocimetry for MATLAB: Accuracy
905 and enhanced algorithms in PIVlab. *J. Open Res. Softw.* **9**, 12 (2021).
906 44. Mayer, M., Depken, M., Bois, J. S., Jülicher, F. & Grill, S. W. Anisotropies in
907 cortical tension reveal the physical basis of polarizing cortical flows. *Nature* **467**,
908 617–621 (2010).
909 45. Willis, J. H., Munro, E., Lyczak, R. & Bowerman, B. Conditional dominant
910 mutations in the Caenorhabditis elegans gene act-2 identify cytoplasmic and muscle
911 roles for a redundant actin isoform. *Mol. Biol. Cell* **17**, 1051–1064 (2006).

912 46. Ozugergin, I., Mastronardi, K., Law, C. & Piekny, A. Diverse mechanisms regulate
913 contractile ring assembly for cytokinesis in the two-cell Caenorhabditis elegans
914 embryo. *J. Cell Sci.* **135**, (2022).
915 47. Bell, K. R. *et al.* Novel cytokinetic ring components drive negative feedback in
916 cortical contractility. *Mol. Biol. Cell* **31**, 1623–1636 (2020).
917 48. Pinheiro, D. *et al.* Transmission of cytokinesis forces via E-cadherin dilution and
918 actomyosin flows. *Nature* **545**, 103–107 (2017).
919 49. di Pietro, F. *et al.* Systematic analysis of RhoGEF/GAP localizations uncovers
920 regulators of mechanosensing and junction formation during epithelial cell division.
921 *Curr. Biol.* **33**, 858-874.e7 (2023).
922 50. Jaffe, A. B., Kaji, N., Durgan, J. & Hall, A. Cdc42 controls spindle orientation to
923 position the apical surface during epithelial morphogenesis. *J. Cell Biol.* **183**, 625–
924 33 (2008).
925 51. Overeem, A. W., Bryant, D. M. & van IJzendoorn, S. C. D. Mechanisms of apical-
926 basal axis orientation and epithelial lumen positioning. *Trends Cell Biol.* **25**, 476–
927 485 (2015).
928 52. Wang, T., Yanger, K., Stanger, B. Z., Cassio, D. & Bi, E. Cytokinesis defines a
929 spatial landmark for hepatocyte polarization and apical lumen formation. *J. Cell Sci.*
930 **127**, 2483–2492 (2014).
931 53. Schlüter, M. A. *et al.* Trafficking of Crumbs3 during cytokinesis is crucial for lumen
932 formation. *Mol. Biol. Cell* **20**, 4652–4663 (2009).
933 54. Moyer, J. H. *et al.* Candidate gene associated with a mutation causing recessive
934 polycystic kidney disease in mice. *Science* **264**, 1329–1333 (1994).

935 55. Brenner, S. The genetics of Caenorhabditis elegans. *Genetics* **77**, 71–94 (1974).
936 56. Dickinson, D. J., Ward, J. D., Reiner, D. J. & Goldstein, B. Engineering the
937 Caenorhabditis elegans genome using Cas9-triggered homologous recombination.
938 *Nat. Methods* **10**, 1028–1034 (2013).
939 57. Sugioka, K. *et al.* Centriolar SAS-7 acts upstream of SPD-2 to regulate centriole
940 assembly and pericentriolar material formation. *Elife* **6**, e20353 (2017).
941 58. Ahringer, J. Reverse genetics. *WormBook* (2006) doi:10.1895/wormbook.1.47.1.
942 59. Edgar, L. G. & Goldstein, B. Culture and Manipulation of Embryonic Cells.
943 *Methods Cell Biol.* **107**, 151–175 (2012).
944 60. Hsu, C. R., Xiong, R. & Sugioka, K. In Vitro Reconstitution of Spatial Cell Contact
945 Patterns with Isolated Caenorhabditis elegans Embryo Blastomeres and Adhesive
946 Polystyrene Beads. *J. Vis. Exp.* (2019) doi:10.3791/60422.
947 61. Shelton, C. A. & Bowerman, B. Time-dependent responses to glp-1-mediated
948 inductions in early C. elegans embryos. *Development* **122**, 2043–2050 (1996).
949 62. Schindelin, J. *et al.* Fiji: an open-source platform for biological-image analysis. *Nat.*
950 *Methods* **9**, 676–682 (2012).
951 63. Biot, E. *et al.* A new filter for spot extraction in n-dimensional biological imaging.
952 in *2008 5th IEEE International Symposium on Biomedical Imaging: From Nano to*
953 *Macro* 975–978 (2008).
954 64. Legland, D., Arganda-Carreras, I. & Andrey, P. MorphoLibJ: integrated library and
955 plugins for mathematical morphology with ImageJ. *Bioinformatics* **32**, 3532–3534
956 (2016).

65. Thévenaz, P., Ruttimann, U. E. & Unser, M. A pyramid approach to subpixel registration based on intensity. *IEEE Trans. Image Process.* **7**, 27–41 (1998).

66. Royer, L. A. *et al.* ClearVolume: open-source live 3D visualization for light-sheet microscopy. *Nat. Methods* **12**, 480–481 (2015).

67. Harris, C. R. *et al.* Array programming with NumPy. *Nature* **585**, 357–362 (2020).

68. McKinney, W. Data Structures for Statistical Computing in Python. in *Proceedings of the 9th Python in Science Conference* (SciPy, 2010). doi:10.25080/majora-92bf1922-00a.

69. Quarteroni, A., Sacco, R. & Saleri, F. *Numerical Mathematics*. (Springer Science & Business Media, 2010).

Figure 1 (Hsu, Sangha, Fan, et al.)

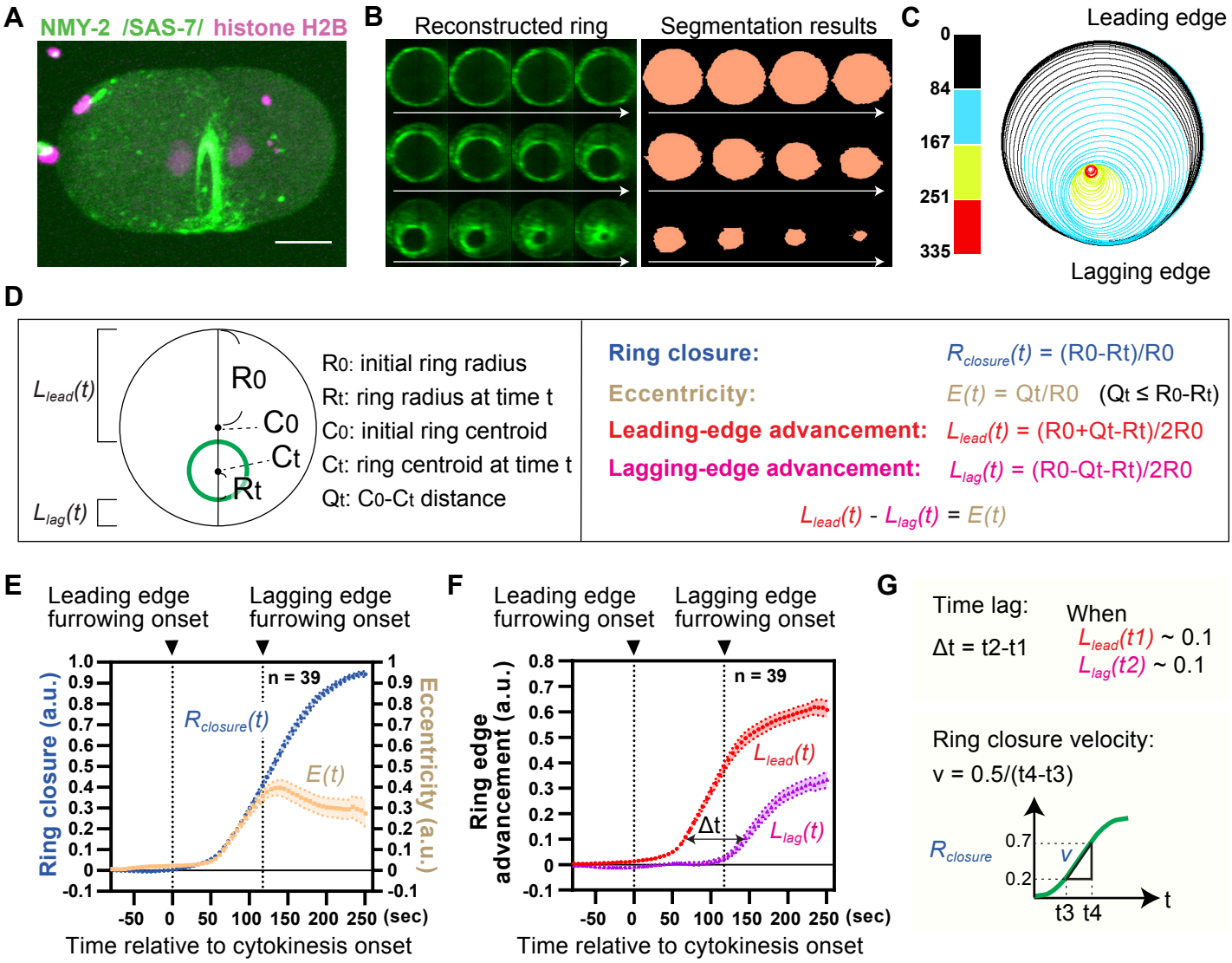

Figure 1. Quantitative analysis of asymmetric contractile ring closure in the *C. elegans* zygote. (**A**) Asymmetric contractile ring closure in *C. elegans* zygote. NMY-2::GFP (green, non-muscle myosin II), GFP::SAS-7 (green, centriole) and histone H2B::mCherry (magenta, chromosome) are shown. In this and subsequent figures, anterior and posterior are to the left and right, respectively. (**B**) Computationally reconstructed ring and segmentation results. The top left image shows cytokinesis onset, and the second and third rows highlight the advancement of the leading and lagging edges, respectively. See Fig S1 for method and full frame images. (**C**) Trajectory of ring constriction. Outlines of the contractile ring during cytokinesis are plotted based on the segmentation results. The color coding indicates time relative to cytokinesis onset. (**D**) Geometric analysis of the contractile ring closure. Eccentricity and ring edge advancement are the degree of ring off-centering and the distance between the ring edge and initial ring perimeter, respectively. (**E**) Mean ring closure and eccentricity. (**F**) Mean ring edge advancement. Lagging furrowing onset was defined as the timing when the $L_{lag}(t)$ exceeded 0.02 (2% relative to initial ring size). (**G**) Definitions of time lag and ring closure velocity (See text). Times are relative to cytokinesis onset. Error bands indicate 95% confidence intervals. Scale bars, 10 μm.

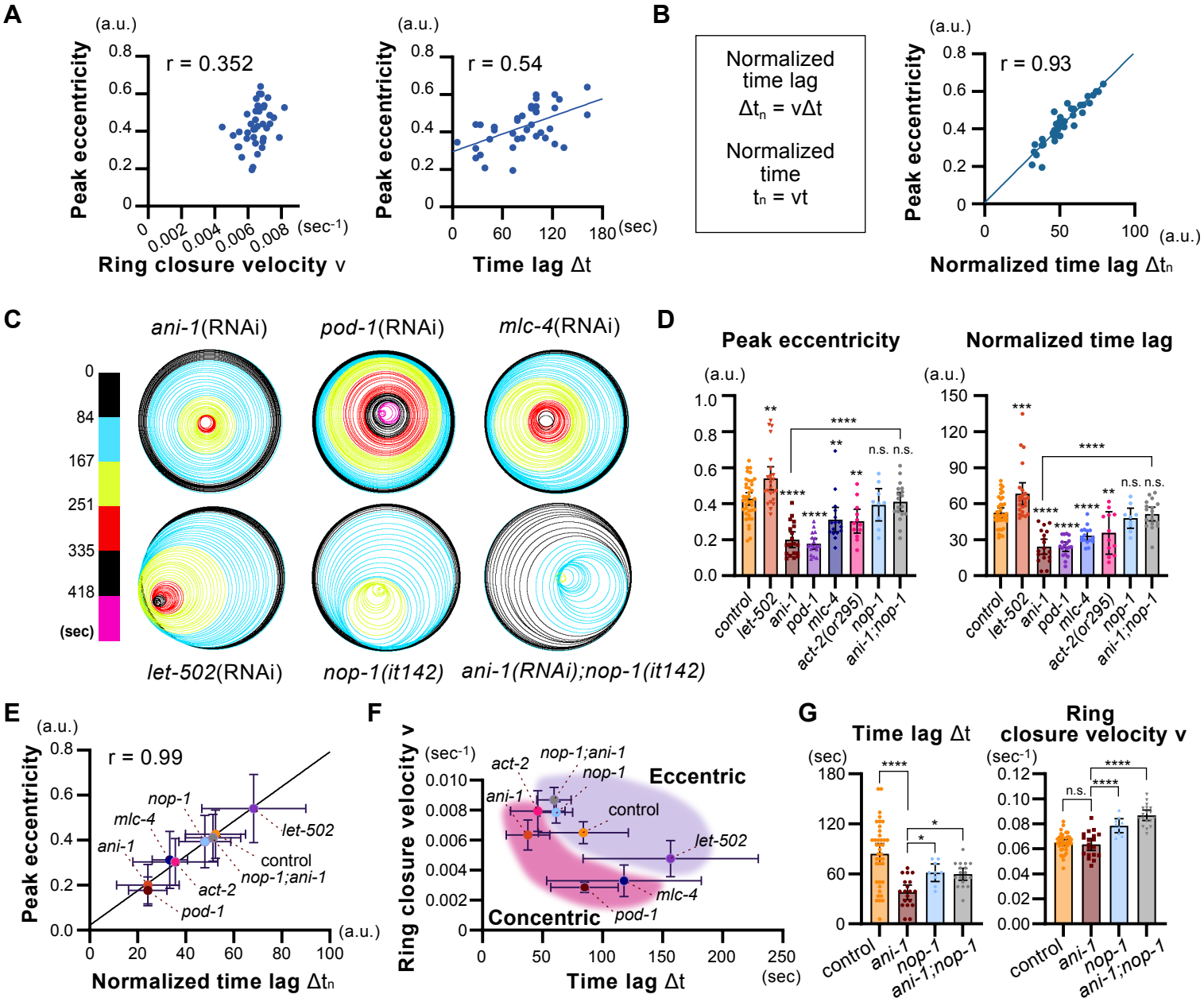

Figure 2. Ring closure velocity and a delay in lagging edge furrowing collectively determine the ring eccentricity.

(**A**) Relationship among peak eccentricity, ring closure velocity, and time lag in normal cells. (B) Relationship between peak eccentricity and normalized time lag in normal cells. (C) Ring trajectories of different RNAi and mutant backgrounds. (D) Peak eccentricity and normalized time lag in different backgrounds. (E) Relationship between peak eccentricity and normalized time lag in different backgrounds. (F) The relationship between ring closure velocity and time lag in different backgrounds. (G) Time lag and ring closure velocity. Times are relative to cytokinesis onset. Error bars indicate 95% confidence intervals except for panel E and F, in which standard deviations were shown. The value r reperesents Pearson's correlation coeffiencient. P-values were calculated using one-way ANOVA followed by Holm-Sidak's multiple comparison test. Scale bars, 10 μm.

Figure 3 (Hsu, Sangha, Fan, et al.)

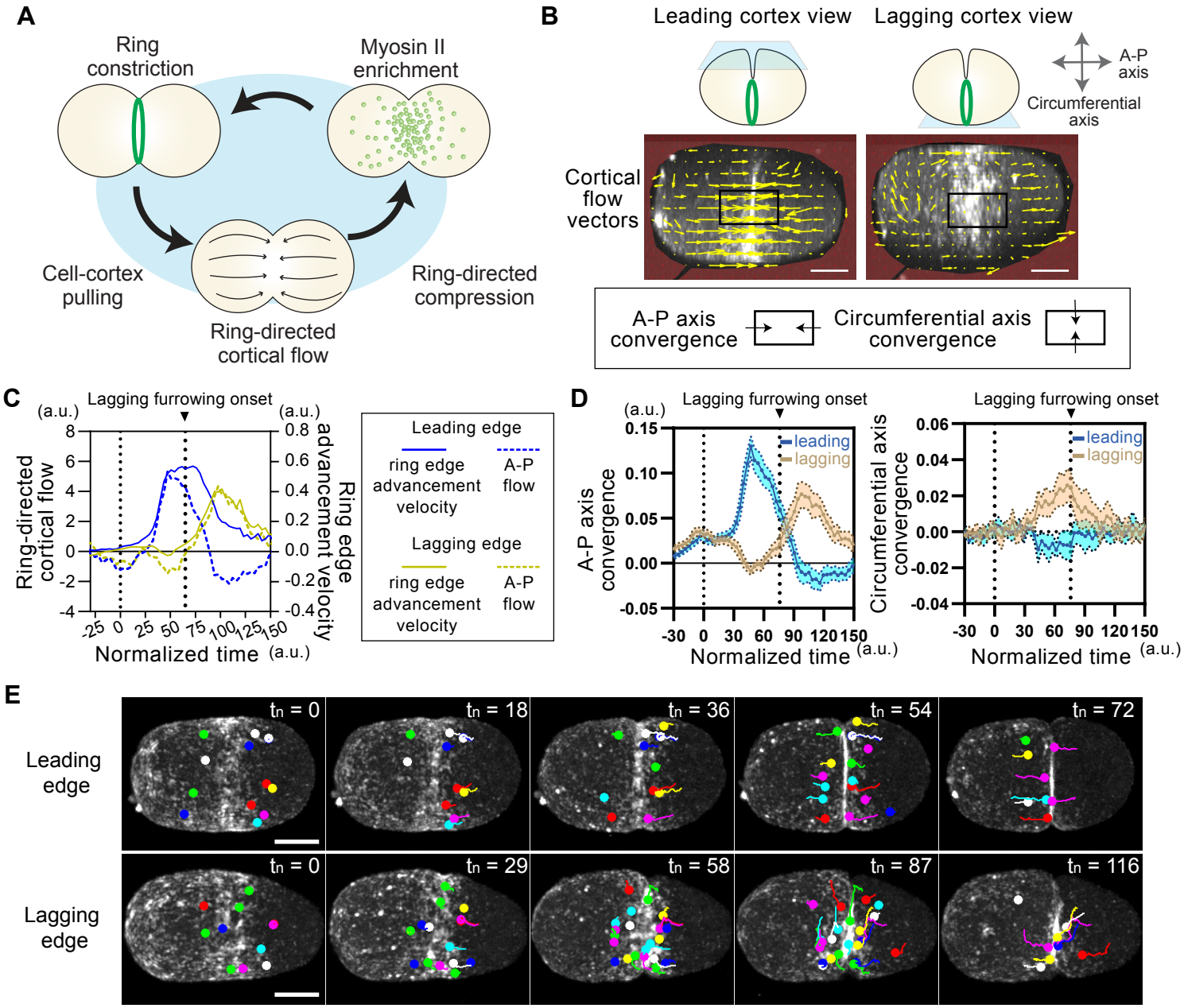

Figure 3. Reduced ring-directed cortical flow at the lagging cell cortex accompanies circumferential-axis cortical flow.

(**A**) A cortical flow-dependent positive feedback model in the contractile ring assembly. Ring-dependent cell cortex pulling generates ring-directed cortical flow and induces ring-directed compression. Resulted myosin enrichment to the ring further facilitates ring constriction. (**B**) Measurement of cortical flow. Leading and lagging cortex views were generated by computationally rotating 4D timelapse data. Cortical flow vectors were estimated using particle image velocimetry (yellow arrows). Convergence of cortical flow vectors were calculated to estimate the influx of cortical flow within the equatorial ROI (black boxes). (**C**) The relationship between ring edge advancement and ring-directed cortical flow. Cortical flow in the area anterior to the ring is shown. (**D**) A-P axis convergence and circumferential axis convergence in leading and lagging cell cortices. (**E**) Myosin foci tracking during cytokinesis. Scale bars, 10 μm.

Figure 4 (Hsu, Sangha, Fan, et al.)

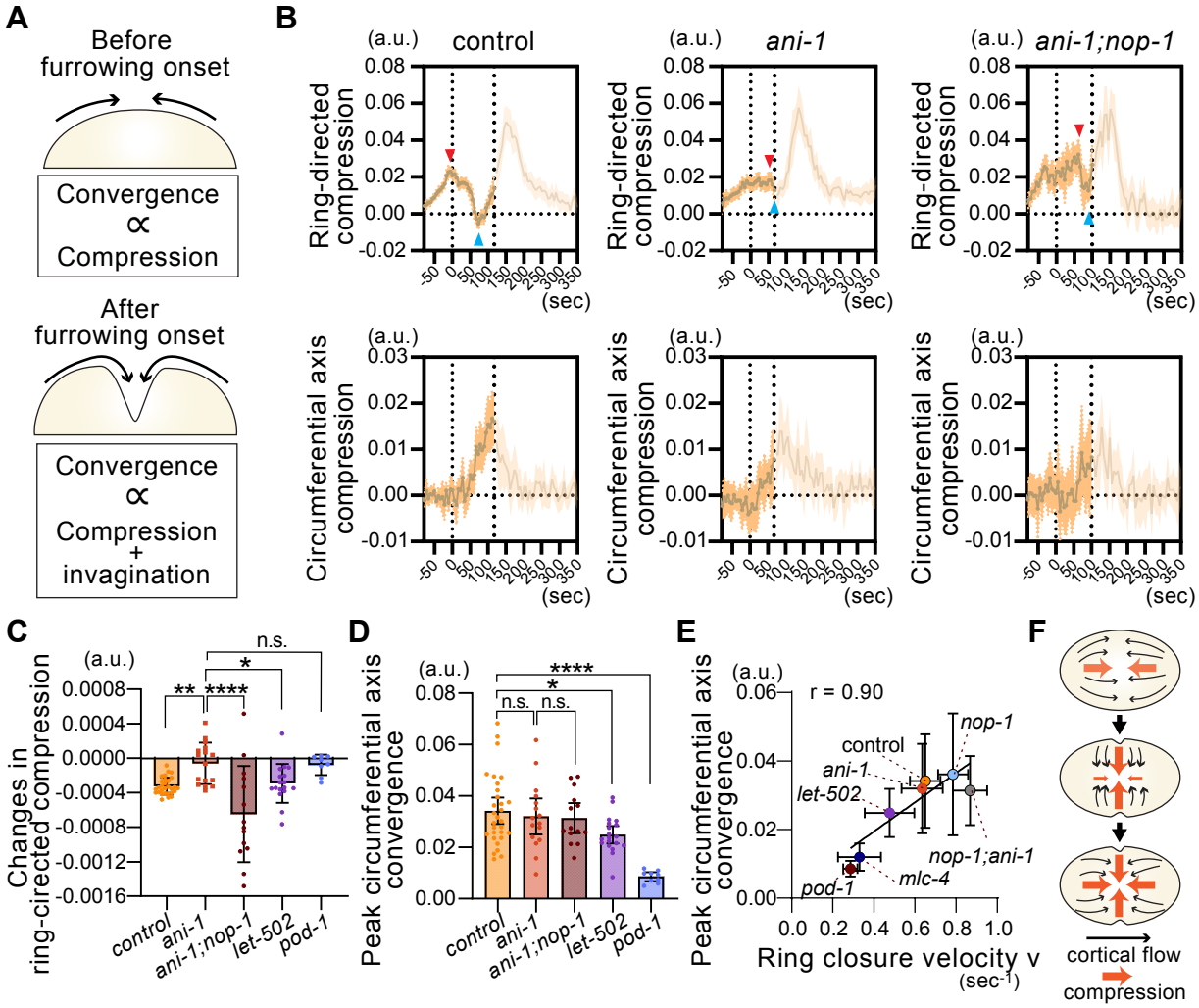

Figure 4. Cells undergoing asymmetric ring closure exhibit polarized mechanical loading at the lagging cortex.

(**A**) Inferring cortical mechanics from cortical convergence data. Before furrowing onset, cortical convergence is proportional to the cortical compression. After furrowing onset, convergence is proportional to the sum of compression and invagination. (**B**) Cortical compression at the lagging equatorial cell cortex. Mean cortical flow convergence before lagging edge furrowing onset was shown. The transparent parts of graphs show the convergence after the furrowing onset. Red and blue arrowheads indicate local maxima and minima between cytokinesis onset (left dotted line) and lagging edge furrowing onset (right dotted line) in each graph. (**C**) Reduction rate of ring-directed compression at the lagging equatorial cortex. (**D**) Peak circumferential axis convergence at the lagging equatorial cortex. (**E**) Relationship between peak circumferential axis convergence and ring closure velocity. The value r represents Pearson's correlation coefficient. (**F**) Summary of the cortical flow and cortical compression at the lagging equatorial cell cortex. Ring-directed compression decreases as the circumferential compression increases. P-values were calculated using one-way ANOVA followed by Holm-Sidak's multiple comparison test.Times are relative to cytokinesis onset. Error bands and bars indicate 95% confidence intervals. Scale bars, 10 μm.

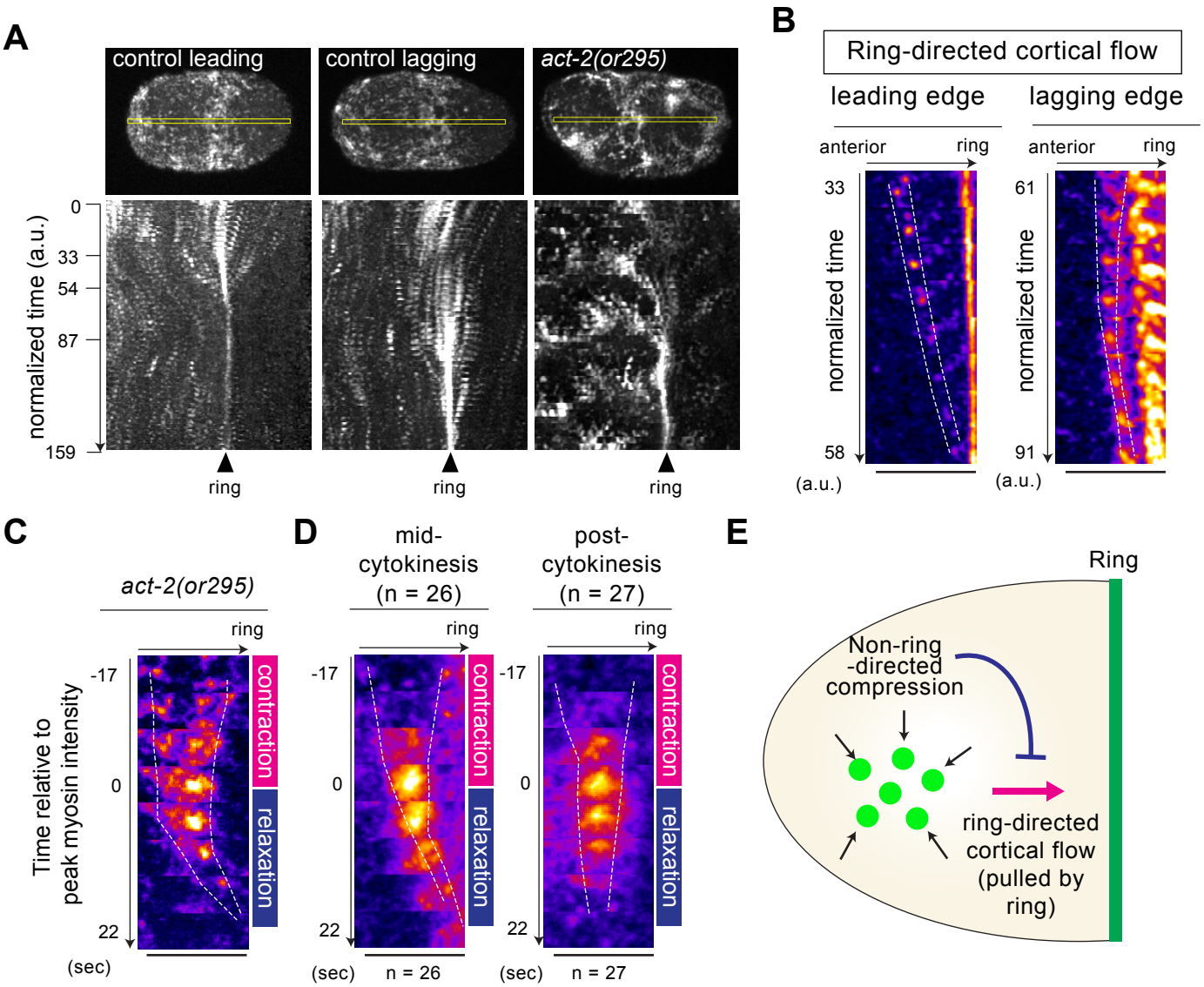

Figure 5. Non-ring-directed cortical compression suppresses ring-directed cortical flow. (**A**) Kymographs of cortical myosin. Yellow boxes in the top images were used to generate kymographs. (**B**) Ring-directed cortical flow in control zygotes. Leading edge shows consistent flow while the lagging edge flow is preceded by the stabilization. (**C**) Ring-directed cortical flow in act-2 mutant zygotes. A myosin focus movement during contraction and relaxation of the area behind the ring was shown. (**D**) Averaged ring-directed flow in act-2 mutant zygotes. (**E**) The mechanism of compression-dependent suppression of the ring-directed cortical flow. While ring-directed compression promotes the ring assembly, non-ring-directed compression suppresses the ring-directed cortical flow. Times are relative to cytokinesis onset. Scale bars, 10 μm.

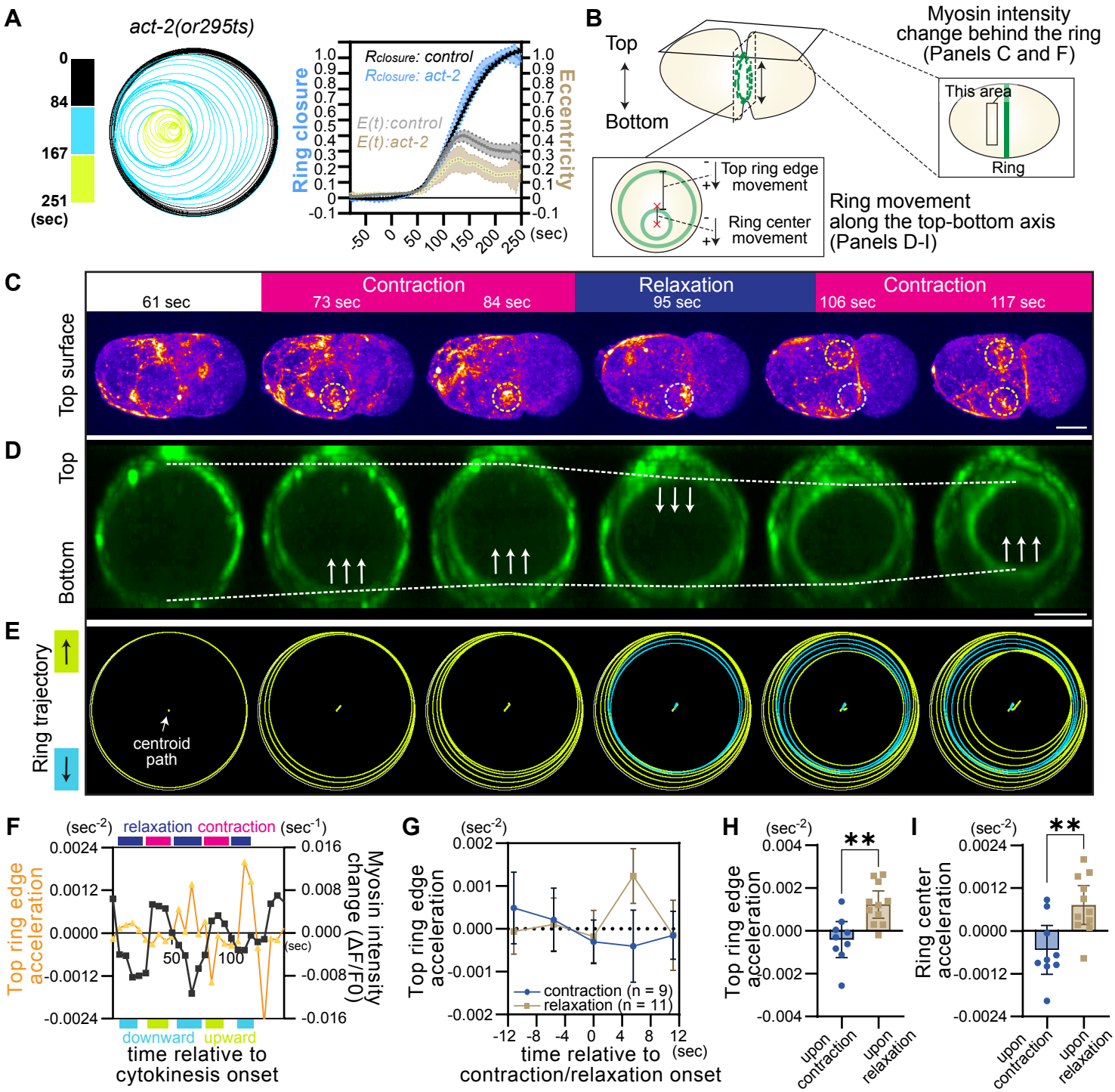

Figure 6. Non-ring-directed cortical compression delays ring edge advancement without suppressing ring constriction.

(**A**) Contractile ring trajectory of a single *act-2(or295ts)* mutant (left panel) and the mean values of ring closure and eccentricity (graph). (**B**) Planes shown in (C-E). Myosin intensity change indicates contraction and relaxation. (**C**) NMY-2::GFP at the top surface during cytokinesis. Yellow and light blue dotted circles indicate the area exhibiting contraction and relaxation, respectively. (**D**) Ring en face view of the same embryo shown in panel C. Dotted lines indicate top and bottom limits of the contractile ring. Arrows indicate the movement of the ring limit. (**E**) Ring trajectories of the contractile ring shown in (D). Top- and bottom-oriented movements are shown in yellow and blue, respectively. (**F**) Relationship between top ring acceleration and myosin intensity changes. Positive ring edge acceleration represents ring ingression toward the bottom surface. (**G**) Top ring edge acceleration upon contraction and relaxation. (**H**) Top ring edge acceleration 5.6 sec after contraction and relaxation. (**I**) Ring center acceleration 5.6 sec after contraction and relaxation. Error bars and bands indicate 95% confidence intervals. Scale bars, 10 μm.

Figure 7 (Hsu, Sangha, Fan, et al.)

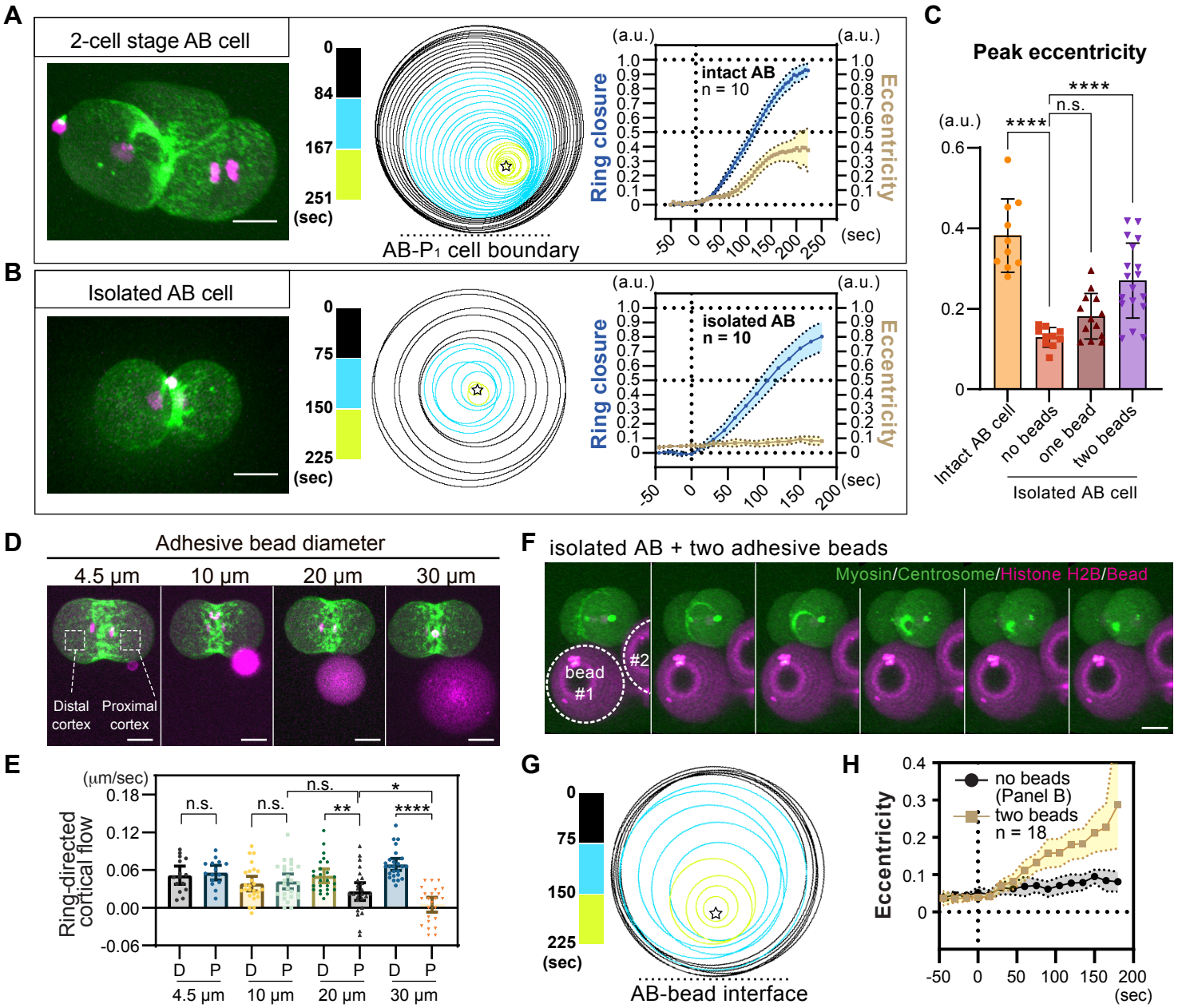

Figure 7. Artificial inhibition of ring-directed cortical flow is sufficient to induce asymmetric ring closure.

(**A, B**) Eccentric ring closure in the intact and isolated AB cell. NMY-2::GFP and mCherry::histone H2B (left), ring trajectories (middle), and ring closure and eccentricity curves (right) are shown. (**C**) Mean peak eccentricity of the contractile ring in the AB cells. (**D, E**) Attachment of different sized adhesive beads to the isolated AB cell. Ring-directed cortical flow were plotted for proximal and distal to the bead attachment site in E. (**F-H**) Oblique view of contractile rings in the bead attached AB cell. Ring trajectory and mean eccentricity are shown in G and H, respectively. Times are relative to cytokinesis onset. Error bands and bars indicate 95% confidence intervals. Scale bars, 10 µm.

Figure 8 (Hsu, Sangha, Fan, et al.)

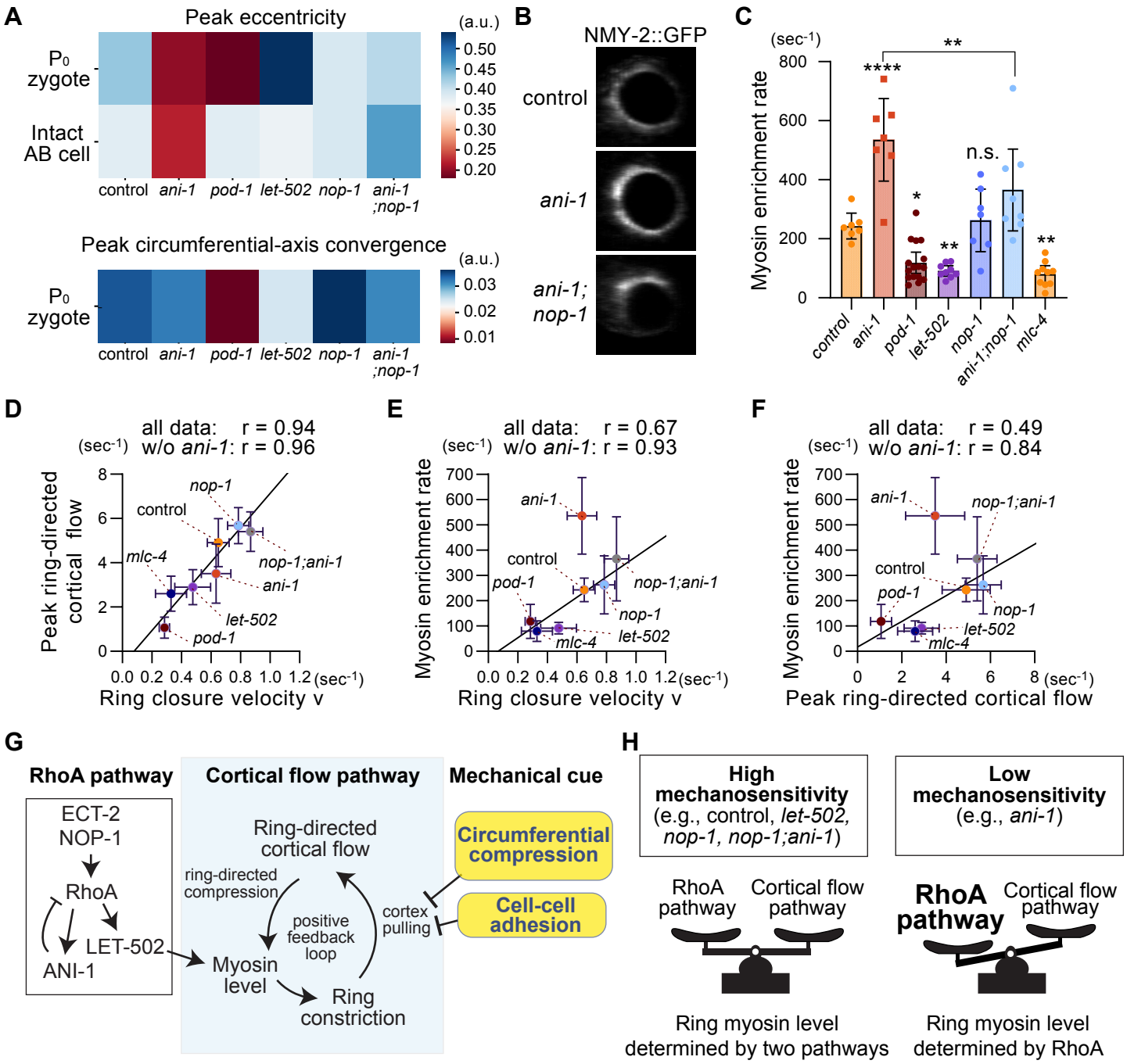

Figure 7. Anillin tunes contractile ring mechanosensitivity.
(**A**) Heatmaps of peak eccentricity and peak circumferential-axis convergence. *ani-1(RNAi)* embryos exhibit defects in asymmetric ring closure in both P0 and AB cells. (**B**, **C**) Contractile ring myosin enrichment. Total myosin signal intensity in the ring (B) was used to estimate myosin enrichment rate in (C). (**D**-**F**) Relationship among ring closure velocity, peak ring-directed cortical flow, and myosin enrichment rate. (**G**) Proposed model of contractile ring-dependent mechanosensation. (**H**) Proposed model of Anillin-dependent tuning of contractile ring mechanosensitivity. Error bars indicate 95% confidence intervals. Scale bars, 10 µm. p-values were calculated by one-way ANOVA with Holm-Sidak's multiple comparison test.